JGR Solid Earth

RESEARCH ARTICLE
10.1029/2018JB017025

Thermochemical Heterogeneity and Density of Continental and Oceanic Upper Mantle in the European-North Atlantic Region

Alexey Shulgin[1] and **Irina M. Artemieva**[1]

[1]CEED, University of Oslo, Oslo, Norway

Key Points:
- Density structure of cratonic mantle suggests strong metasomatic reworking
- Superdeep basins require the presence of 10–20% of eclogites in the mantle
- Mantle temperature anomaly around Iceland is at the limit of seismic detection

Supporting Information:
- Supporting Information S1
- Data Set S1
- Data Set S2

Correspondence to:
A. Shulgin and I. M. Artemieva,
alexey.shulgin@geo.uio.no;
iartemieva@gmail.com

Citation:
Shulgin, A., & Artemieva, I. M. (2019). Thermochemical heterogeneity and density of continental and oceanic upper mantle in the European-North Atlantic region. *Journal of Geophysical Research: Solid Earth*, *124*, 9280–9312. https://doi.org/10.1029/2018JB017025

Received 14 NOV 2018
Accepted 23 JUL 2019
Accepted article online 31 JUL 2019
Published online 22 AUG 2019

Abstract We present a new model, EUNA-rho, for the density structure of the continental and oceanic upper mantle based on 3-D tesseroid gravity modeling. On continent, there is no clear difference in lithospheric mantle (LM) density between the cratonic and Phanerozoic Europe, yet an ~300-km-wide zone of a high-density LM along the Trans-European Suture Zone may image a paleosubduction. Kimberlite provinces of the Baltica and Greenland cratons have a low-density (3.32 g/cm^3) mantle where all non-damondiferous kimberlites tend to a higher-density (3.34 g/cm^3) anomalies. LM density correlates with the depth of sedimentary basins implying that mantle densification plays an important role in basin subsidence. A very dense (3.40–3.45 g/cm^3) mantle beneath the superdeep platform basins and the East Barents shelf requires the presence of 10–20% of eclogite, while the West Barents Basin has LM density of 3.35 g/cm^3 similar to the Variscan massifs of western Europe. In the North Atlantics, south of the Charlie Gibbs fracture zone (CGFZ) mantle density follows half-space cooling model with significant deviations at volcanic provinces. North of the CGFZ, the entire North Atlantics is anomalous. Strong low-density LM anomalies ($< -3\%$) beneath the Azores and north of the CGFZ correlate with geochemical anomalies and indicate the presence of continental fragments and heterogeneous melting sources. Thermal anomalies in the upper mantle averaged down to the transition zone are 100–150 °C at the Azores and can be detected seismically, while a <50 °C anomaly around Iceland is at the limit of seismic resolution.

1. Introduction

Thermochemical heterogeneity of the upper mantle is a fundamental problem in geodynamics. Both temperature and composition affect physical parameters (seismic velocities, elastic moduli, and density) measured in remote geophysical surveys (Jordan, 1975, 1979; Lee, 2003; Schutt & Lesher, 2006; Simmons et al., 2009), yet geodynamic modeling and understanding of secular evolution of the Earth require independent information on thermal and compositional variations in the upper mantle, which are also directly linked to and reflect the processes of formation and evolution of the overlaying crust. Thermochemical buoyancy of the lithosphere (James et al., 2004; Jordan, 1988; Kelly et al., 2003; Lee et al., 2004) contributes to the craton stability over long geological times (Doin et al., 1997; Eaton & Perry, 2013; Lee et al., 2004; Lenardic & Moresi, 1999; Shapiro et al., 1999; Sleep, 2005) and controls the initialization and the style of subduction (O'Neill et al., 2007; Sizova et al., 2010), therefore affecting the style of mantle convection (Bercovici et al., 2000; Sleep, 2005). Furthermore, large-scale topography features also depend on density variations in the upper mantle (Steinberger, 2016) which affect the gravity field and geoid (Cazenave, 1994; Panasyuk & Hager, 2000; Ricard et al., 1993; Shapiro et al., 1999).

Lateral and vertical variability of in situ upper mantle density structure may be inferred from a joint inversion of seismic and gravity data (Deschamps et al., 2002; Forte & Perry, 2000; Tondi et al., 2012), yet the major problem is the nonuniqueness of the relation between seismic velocities and density (Barton, 1986; Brocher, 2005; Deschamps et al., 2001; Lee, 2003). The approach does not allow for separating thermal and compositional effects on physical properties of the mantle, which requires additional assumptions either on mantle temperatures or on composition. Alternatively, gravity and free-board modeling are used to model global and regional patterns of density variations in the upper mantle (Molnar et al., 2015; Mooney & Vidale, 2003), and compositional variations in mantle density can be calculated if thermal structure of the lithospheric mantle (LM) is known. One approach involves subtracting gravitational effect of crustal heterogeneity from the observed gravity field (Artemjev et al., 1994; Artemieva et al., 2019; Herceg et al., 2016; Kaban &

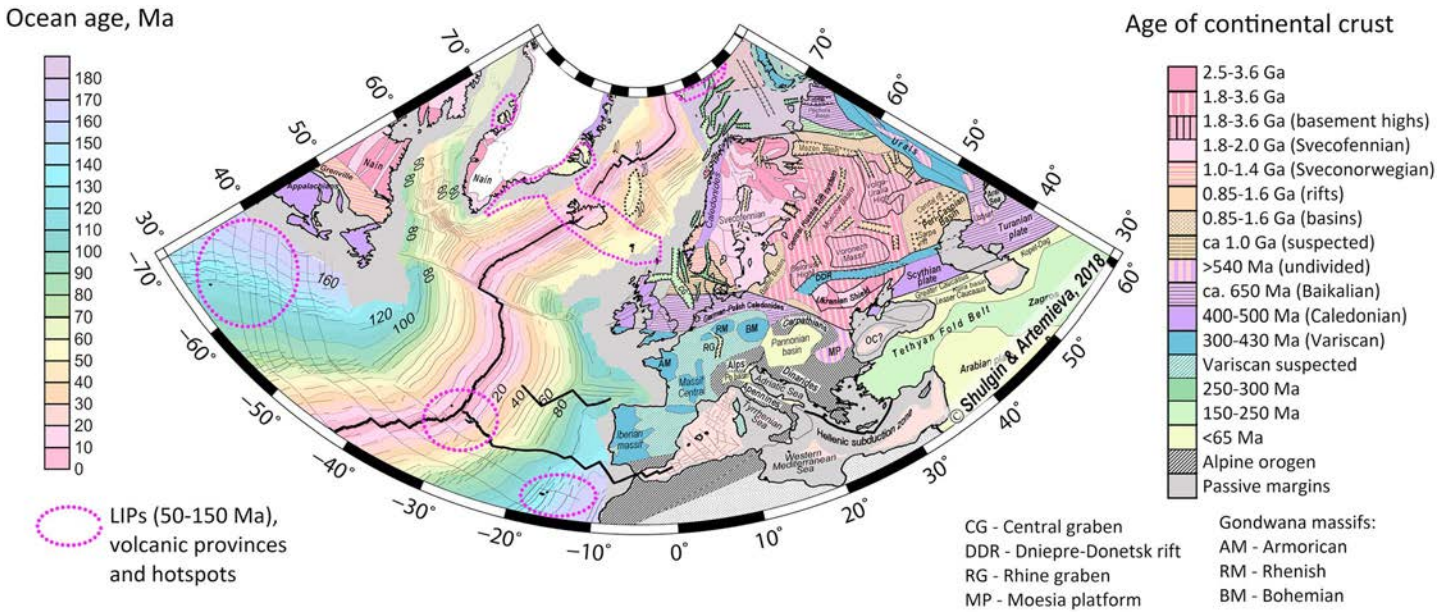

Figure 1. Tectonic map for Europe and the North Atlantics (modified after Artemieva & Thybo, 2013).

Mooney, 2001; Kaban et al., 2003, 2016; Mooney & Kaban, 2010; Yegorova & Starostenko, 2002), and the other includes mantle density calculation from lithosphere buoyancy in regions that are close to isostatic equilibrium (Artemieva, 2003; Artemieva & Vinnik, 2016; Cherepanova & Artemieva, 2015; Mooney & Vidale, 2003). In both cases the results are critically dependent on the quality and resolution of the crustal model (Herceg et al., 2016; Kaban & Schwintzer, 2001), which necessitates the development of high-quality regional seismic models for the crust (Artemieva & Thybo, 2013; Cherepanova et al., 2013; Grad et al., 2009; Kennett et al., 2011; Tesauro et al., 2014; Xia et al., 2017). For example, a global gravity modeling demonstrated the presence of strong low-density anomalies (−0.10–0.05 g/cm^3) in the subcontinental lithospheric mantle (SCLM) of the cratons (Kaban et al., 2003), but the resolution is insufficient to resolve reliably intracratonic density variations due to limitations of a global model of the crustal structure used in calculations.

Regional studies for the SCLM density structure are available for Eurasia (Artemjev et al., 1994), the East European craton (Artemieva, 2003), Europe and the North Atlantics (Yegorova & Starostenko, 2002), North America (Kaban & Mooney, 2001; Mooney & Kaban, 2010), Siberia (Artemieva et al., 2019; Cherepanova & Artemieva, 2015), Asia (Kaban et al., 2016), and southern Africa (Artemieva & Vinnik, 2016). The results of these studies are in overall agreement with global geochemical observations on secular variations in SCLM density (Gaul et al., 2000; Griffin et al., 1998): Cratonic LM is typically 0.5–2% less dense than the asthenospheric mantle, with significant lateral variations within and between the cratons (Griffin et al., 2004). However, a comparison of different continental regions calculated by different groups is challenging, in part due to fundamentally different assumptions on thermal structure of the upper mantle and on the depth range to which mantle gravity anomalies are confined. In particular, one may use thermal models constrained by surface heat flux and xenolith geothermobarometry and resolved on a 1° × 1° spatial grid (Artemieva et al., 2006; Artemieva & Mooney, 2001) or may constrain mantle temperatures from seismic tomography (Goes et al., 2000, 2005; Kaban et al., 2016), despite that geophysical studies indicate the presence of a strong nonthermal (compositional, melt, water, and grain size) component in seismic velocity variations (Afonso & Schutt, 2012; Artemieva, 2009; Faul & Jackson, 2005; Godey et al., 2004; Lee, 2003; Zhu et al., 2013), and lateral resolution of these models is significantly less than 1° × 1° (Foulger et al., 2013).

The number of studies for density variations in the oceanic upper mantle remains limited with major focus on ocean cooling models and regional deviations from them (Cadio & Korenaga, 2014; Cazenave, 1994;

Cowie & Kusznir, 2018; Deschamps et al., 2002; Kaban et al., 1999; Panasyuk & Hager, 2000). It is commonly assumed that the density structure of oceanic upper mantle is controlled chiefly by ocean cooling, yet regional geochemical studies from ocean hot spots indicate significant compositional heterogeneity of the mantle melting source (Harrison et al., 2017; Korenaga & Kelemen, 2000; Simon et al., 2008; Widom, 2002). Regional gravity studies of the upper mantle are limited mostly to regions of continent-ocean transition, where active seismic profiles provide information on the crustal structure (Maystrenko & Scheck-Wenderoth, 2009; Tan et al., 2018).

In this study we perform gravity modeling with focus on density heterogeneity of the upper mantle in Europe and the North Atlantic Ocean (70°W to 60°E, 30–80°N; Figures 1 and 2a). The region includes a mosaic of continental terranes with ages ranging from Archean to Cenozoic and the oceanic domain with the oldest ages of circa 180 Ma and with a number of volcanic provinces and hot spots, including Iceland, the Azores, the off-shore Meteor hot spot track, and the North Atlantic Large Igneous Province (LIP) (Figure 1). Most of the regions are not isostatically compensated, and therefore calculations based on free-board modeling and lithosphere buoyancy cannot be used. We use a regional seismic model for the crust (EUNAseis; Artemieva & Thybo, 2013) and calculate its gravitational effect. The difference between the observed gravity and the crustal gravity is next interpreted in terms of upper mantle density heterogeneity, which we assume to be confined to the LM. To examine compositional heterogeneity of the upper mantle, we use available thermal models for the continental and oceanic domains. Yet by comparing the North Atlantic Ocean to "normal oceans" where bathymetry follows the square-root-of-age pattern, we also calculate thermal anomalies in the oceanic part of the region down to the mantle transition zone. For the continental domain we constrain only compositional heterogeneity of the SCLM. For both the oceanic and the continental domains, we compare the results with geochemical data and seismic tomography models.

2. Crustal and Lithosphere Structure

2.1. Crustal Data

Modeling gravity and density anomalies in the upper mantle requires removal of crustal gravitational effect from the observed gravity field, and crustal models based on gravity data (e.g., Haase et al., 2017) cannot be used in such type of modeling. For example, the CRUST1.0 global crustal model (Laske et al., 2013) constrains crustal structure by gravity data in regions without seismic data. It also shows significant deviations from regional seismic profiles, for example, ~10 km for the Moho depth in the oceanic domain around Iceland (Artemieva & Thybo, 2013).

In this study we use an updated regional crustal model EUNAseis (Artemieva & Thybo, 2013), which is based on compilation of seismic reflection/refraction profiles, complemented by seismic receiver function information on the Moho depth in regions with sparse seismic profiles (Table 1). This in particular is the case for Greenland, where we use a P-RF model (Dahl-Jensen et al., 2003) complemented by recent interpretations along the active source seismic profile, TopoGreenland, which covers the region from the east coast of Greenland to the island's center (Kraft et al., 2019; Shulgin & Thybo, 2014). We also updated the EUNAseis model for seismic profiles in the North Atlantic Ocean, where the seismic data coverage is still sparse (Figure S1 in the supporting information). To close large gaps in data coverage, we assign a 7-km-thick oceanic crust with a standard velocity structure to oceanic crust of the North Atlantic Ocean not covered by seismic data.

The EUNAseis model contains detailed information on V_p velocities and thicknesses of five crustal layers: sediments, upper crust, middle crust, lower crust, and high-V_p lowermost crust, digitized along the profiles with spacing of 50 km or less in regions with heterogeneous crust, and complemented by seismic receiver functions on the Moho depth in regions not covered by seismic profiles (Artemieva & Thybo, 2013). To account correctly for a 3-D gravity effect in areas with a sharp change in the crustal structure (Figure 2), the digitized seismic data of the updated EUNAseis model are interpolated to a 0.5° × 0.5° grid. Since the region covers a large range of latitudes, interpolation was done in the equal-distant projection for true metric distances to avoid geometrical distortion during interpolation. The same interpolation procedure was used for all other parameters, and our modeling is performed on a 0.5° × 0.5° grid. Due to a large density contrast between the (depth-integrated) sediments and the mantle, accurate information on the thickness of the sedimentary layer (Figure 2b) is critical for gravity modeling (Herceg et al., 2016). For the North Atlantic oceanic

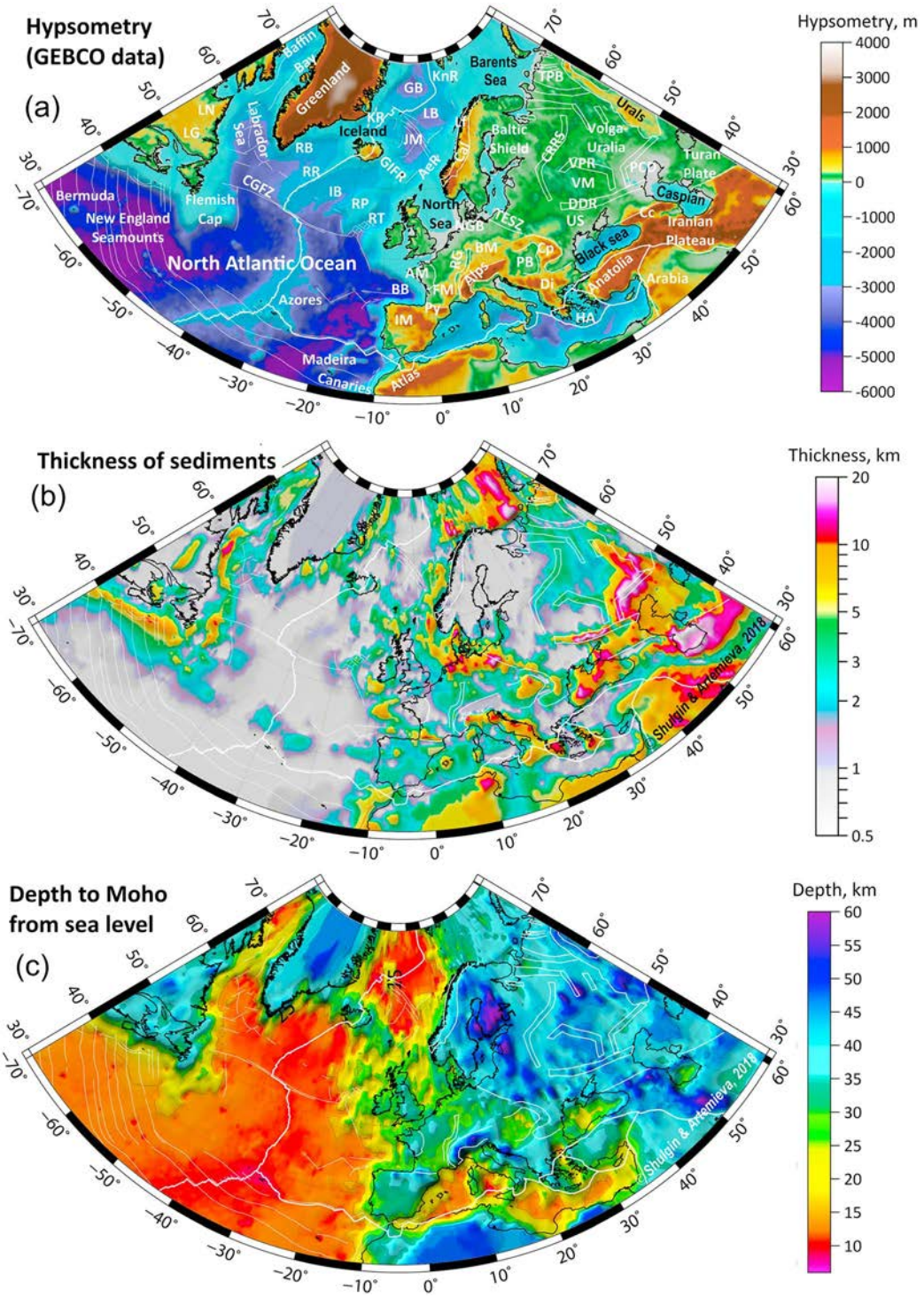

Figure 2. (a) Hypsometry of the study region (based on GEBCO data set, 2010). Plate boundaries, major oceanic fracture zones, and selected continental provinces are shown by white lines. Abbreviations: Ocean: Aer = Aegir paleo-MOR; BB = Bay of Biscay; CGFZ = Charlie-Gibbs Fracture Zone; GB = Greenland Basin; GIFR = Greenland-Faroe-Iceland Ridge; HA = Hellenic subduction arc; IB = Iceland Basin; JM=Jan Mayen block; KnR = Knipovich Ridge; KR = Kolbeinsey Ridge; LB = Lofoten Basin; RB = Reykjanes Basin; RR = Reykjanes Ridge; RP = Rockall Plateau; RT = Rockall Trough. Continent: AM = Armorican massif; BM = Bohemian massif; Cal = Norwegian Caledonides; Cc = Caucasus; Cp = Carpathians; CRRS = Central Russia Rift system; DDR = Dniepre-Donets rift; Di = Dinarides orogen; FM = French Massif Central; IM = Iberian massif; Lf = Lofoten block; LG = Labrador Grenvillian province; LN = Labrador Nain province; NGB = North German Basin; PB = Pannonian Basin; PCD = Peri-Caspian Depression; Py = Pyrenees; RG = Rhine Graben; TESZ = Trans-European Suture Zone; TPB = Timan-Pechora Basin; US = Ukrainian Shield; VM = Voronezh Massif; VPR = Vyatka-Pachelma Rift. (b) Thickness of sediments (see Table 1 for data sources). (c) Depth to Moho from sea level (see Table 1 for data sources).

Table 1
Data Sources for Crustal and Lithosphere Structure

Layer structure	Continental Europe	Arctic shelf	North Atlantic ocean
Thickness of sediments	EXXON (1985); EUNAseis model (Artemieva & Thybo, 2013)	EXXON (1985); Regional data (Drachev et al., 2010); EUNAseis model (Artemieva & Thybo, 2013)	NGDC data (Divins, 2008)
Crustal structure (V_P and thickness in four basement layers)	EUNAseis model (Artemieva & Thybo, 2013)	EUNAseis model (Artemieva & Thybo, 2013)	Updated EUNAseis model (Artemieva & Thybo, 2013); Fixed 7-km-thick crust in regions without seismic data
LAB depth	TC1 model (Artemieva et al., 2006)	Fixed at 110-km depth	Half-space cooling model, based on ocean age; Minimum depth of 40 km is assigned to MOR and very young oceans

Note. LAB = lithosphere-asthenosphere boundary; MOR = mid-ocean ridge.

domain, the thickness of sediments in the EUNAseis database is based on a 5′ NGDC global compilation (Divins, 2008); for the continents and the Arctic shelf the sedimentary thickness is constrained by seismic data and compilation of drilling data by EXXON (1985), which was updated in EUNAseis by a recent compilation for the Arctic Shelf (Drachev et al., 2010).

2.2. Average Crustal Density

Gravity modeling requires information on the crustal density structure. We therefore, convert seismic V_p for each crustal layer in the EUNAseis model to density. A large number of conversion curves have been proposed based on laboratory studies of global, regional and local data (e.g., Ocean Drilling Programme (ODP) data). They all are consistent, especially for metamorphic and igneous rocks (Figure 3a). For the

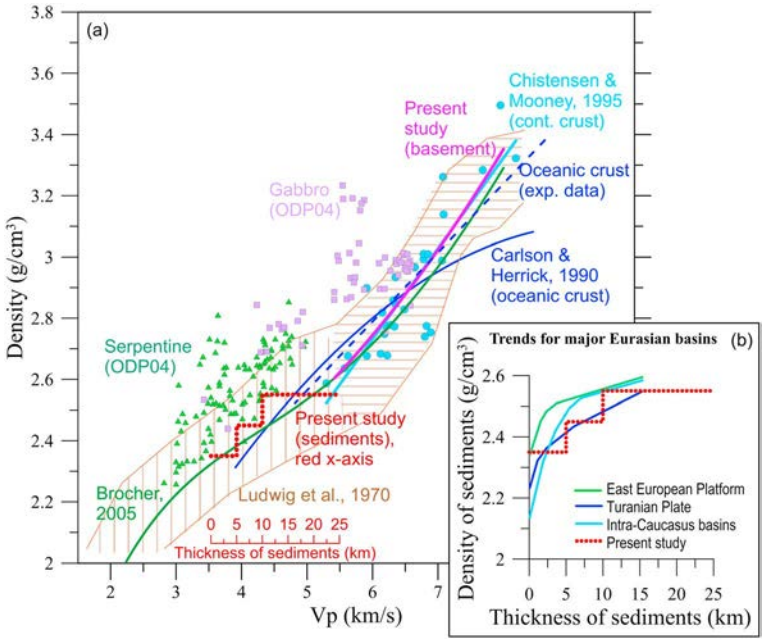

Figure 3. Correlation between seismic V_p and density for crustal rocks. (a) Selected experimental data and commonly used V_p-to-density conversion curves for the crystalline crust (Brocher, 2005; Carlson & Herrick, 1990; Christensen & Mooney, 1995; Ludwig et al., 1970). (b) V_p-to-density conversion curves proposed for some sedimentary basins of Eurasia (Avchan & Oserskaya, 1985). In the present study we use fixed values for sediment density (red line), depending on the thickness of the sedimentary fill.

crystalline crust, we use the conversion based on data of Christensen and Mooney (1995), which is parameterized by the second-order polynomic equation

$$\rho = 2.0855 - 0.0358864 \cdot Vp + 0.0242794 \cdot Vp^2 \quad (1)$$

and provides a close fit to Brocher (2005) for the crystalline crust.

The East European craton is covered by old and dense (meta)sediments and includes several superdeep (>20 km) basins where the lower layers of sediments are likely to have been metamorphosed due to high pressures and temperatures. The region also includes young and shallow on-shore and off-shore basins. It is therefore hardly possible to choose a universal V_p-density conversion curve for all sedimentary basins of the region, as used in previous studies (Yegorova & Starostenko, 2002). Besides no correlation exists between the thickness of sediments and V_p in the sedimentary cover of Europe and the North Atlantic region (Artemieva & Thybo, 2013), indicating significant differences in the density structure of different basins, which depend on regional tectonics and burial history. The same study (Artemieva & Thybo, 2013) did not confirm general trends of density variation with depth proposed for some major sedimentary basins of the ex-USSR (Avchan & Oserskaya, 1985; Oserskaya & Podoba, 1967) and used in some gravity studies of the region (Artemjev et al., 1994; Kaban et al., 2003).

We therefore assign fixed density to the sedimentary layer, depending on the basin depth (Figure 3b) and use the following density values: 2.35 g/cm^3 for basins with <5-km thickness of sediments, 2.45 g/cm^3 for the basin depth between 5 and 10 km, and 2.55 g/cm^3 for thickness of sediments in access of 10 km. Thus, for deep sedimentary basins we effectively create three sedimentary layers with density increasing with depth to account for compaction and for possible metamorphism in the superdeep basins. The adopted values cover the range of commonly assumed values for both deep and shallow basins of Eurasia located in different tectonic settings (Avchan & Oserskaya, 1985; Oserskaya & Podoba, 1967). They are also in agreement with recent studies in the Barents and Kara Seas based on seismic and gravity data which suggest a density increase from 2.20–2.30 g/cm^3 in Quaternary sediments to 2.50–2.55 g/cm^3 in the deep strata (Barrere et al., 2011; Kashubin et al., 2018). We do not use the maximum local values of 2.60 g/cm^3 reported for the western Barents Sea (Barrere et al., 2011), since it is unclear how representative they may be of all deep basins in the study region, and note that a 0.05-g/cm^3 underestimate in density for a 5-km-thick layer will produce a 10-mGal gravity effect, which is well within the overall uncertainty of our modeling. The resulting average density of the crust in Europe-North Atlantics is shown in Figure 4a. It clearly correlates with the thickness of the sedimentary cover (Figure 2b).

2.3. Lithosphere Thickness and Temperature

Residual mantle gravity anomalies (RMG) can be calculated by subtracting the crustal gravitational effect (including water and ice) from the observed gravity field. However, the next step, that is calculation of mantle density from the RMG anomalies, requires knowledge on the thickness of the layer to which density variations (caused by anomalies in temperature and composition) are confined. We assume that most of these anomalies are within the LM, and therefore add the depth to the lithosphere-asthenosphere boundary (LAB) to the model (Figure 4b).

We do not use seismic tomography models to define the LAB for several reasons. (1) Tomography models that cover the entire region provide a significantly different images of the upper mantle velocity structure (Kustowski et al., 2008; Lu et al., 2018; Ritzwoller & Levshin, 1998; Schaeffer & Lebedev, 2013; Schivardi & Morelli, 2009; Villasenor et al., 2001; Weidle & Maupin, 2008; Yang et al., 2007; Zhu et al., 2012), with a significant discrepancy in tomography models for the Arctic region (Lebedev et al., 2018; Levshin et al., 2007) and for different parts of the continental Europe (Hejrani et al., 2017; Kastle et al., 2018; Lippitsch et al., 2003; Pedersen et al., 2013; Silvennoinen et al., 2016). (2) Upper mantle of, at least, some parts of the region is anisotropic (Eken et al., 2012; Fry et al., 2010; Kustowski et al., 2008; Pilidou et al., 2004; Plomerová & Babuška, 2010; Zhu et al., 2015), complicating interpretations of velocity anomalies in terms of the LAB. (3) The LAB is expected to be gradual (Jaupart & Mareschal, 1999; Karato et al., 2015; Kustowski et al., 2008) and therefore it is ambiguous, which velocity perturbation may correspond to the LAB. (4) The resolution (spatial, depth, and amplitude) of the tomography models remains a controversial issue (Foulger et al., 2013) and probably is much more coarse than a 0.5° × 0.5° grid used in our calculations. (5) Finally, to convert

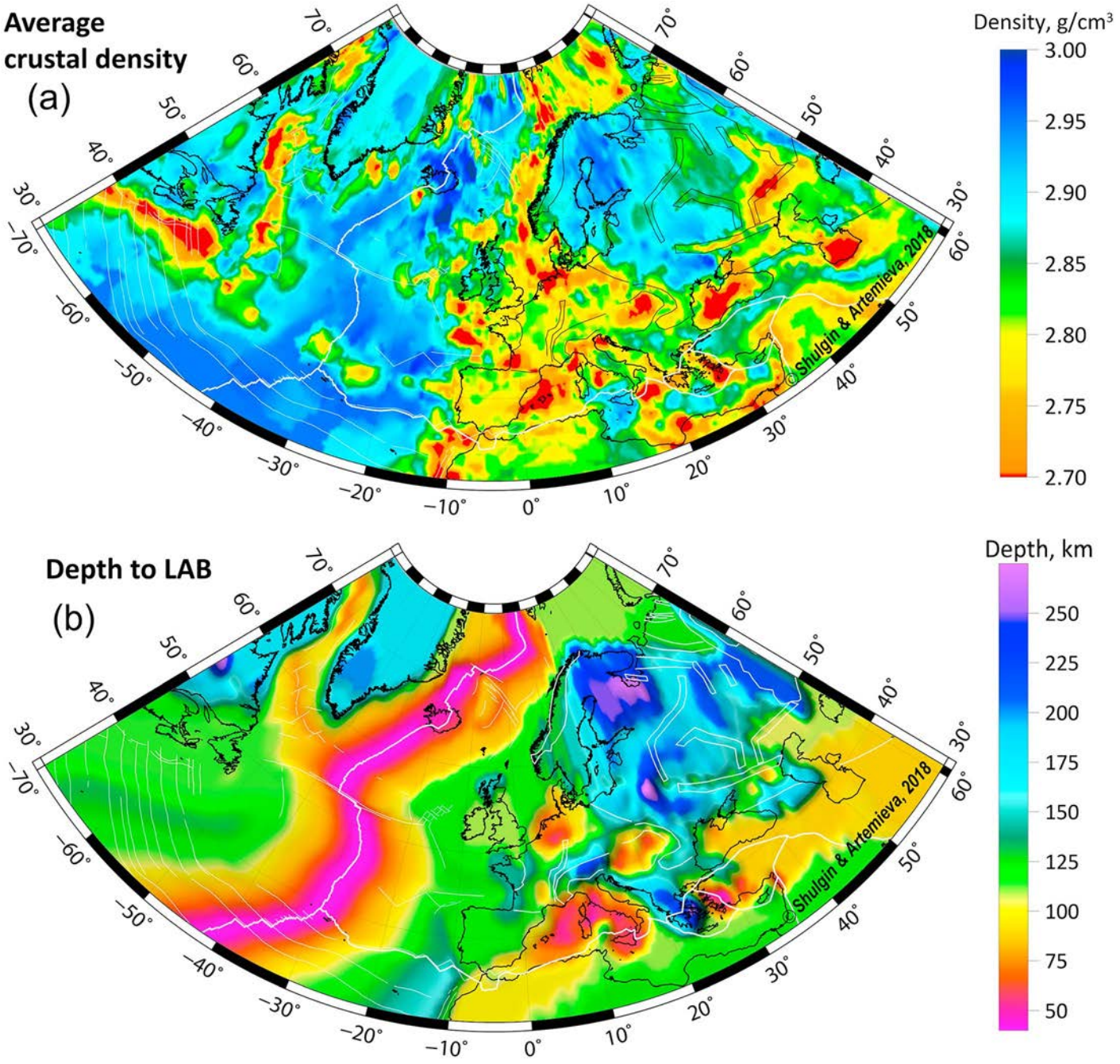

Figure 4. (a) Average density of the crust, including sediments (Figure 2b), but excluding water for oceans and ice cap for Greenland. Density model is based on the conversion curves shown in Figure 3 applied to the EUNAseis crustal model (Artemieva & Thybo, 2013). (b) Depth to the lithosphere-asthenosphere boundary (LAB; see Table 1 for data sources). LAB = lithosphere-asthenosphere boundary.

the calculated in situ mantle densities to room conditions, we need information on upper mantle temperatures. Therefore, we use a thermal model for the LAB depth (Figure 4b).

For the continental domain, we use a part of the global continental thermal model TC1 where the lithosphere base is defined by the depth to a 1300 °C isotherm (Artemieva et al., 2006). The Arctic shelf and other off-shore regions with the continental lithosphere are not included into the TC1 model and we assign them the fixed LAB depth of 110 km (Table 1). This assumption may not be fully correct (Artemieva, 2019) and it affects, in part, our conclusions on the deep structure of the Barents Sea. The choice of the LAB depth is

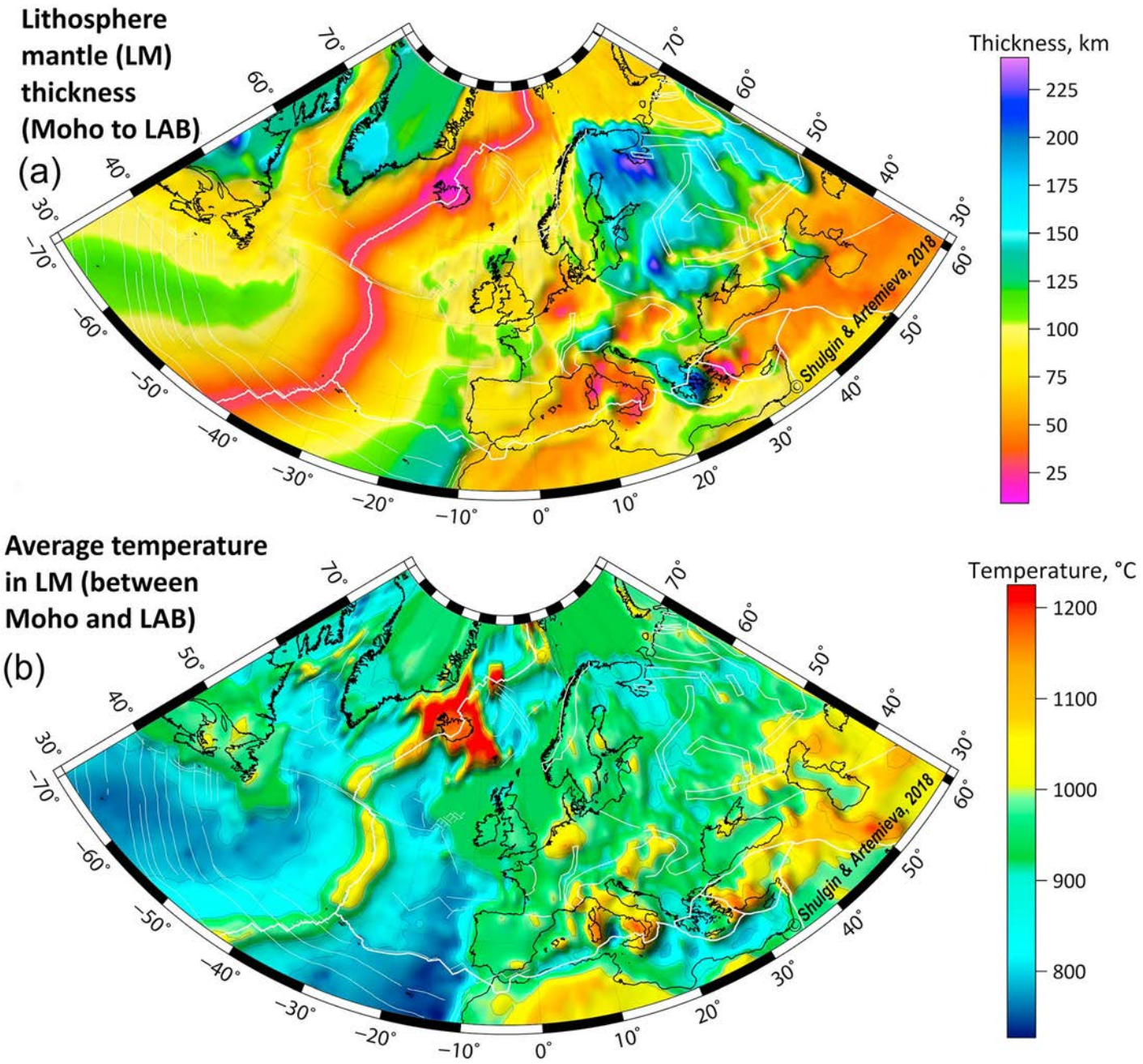

Figure 5. (a) Thickness of lithospheric mantle (LM) calculated as the difference between the LAB depth (Figure 4b) and the Moho depth (Figure 2c). (b) Average temperature of LM, assuming LAB temperature of 1350 °C. Moho temperature for continents is based on the TC1 model (Artemieva et al., 2006); for oceans—computed from linear temperature gradients in the lithosphere assuming thermal conductivity of 2.5 $W \cdot m^{-1} \cdot K^{-1}$ for the crust and 4.0 $W \cdot m^{-1} \cdot K^{-1}$ for LM. High temperature anomalies around Iceland and at the Jan Mayen block are due to the small thickness of LM (Figure 5a) in the proximity to the mid-ocean ridge. LAB = lithosphere-asthenosphere boundary.

based on the following considerations. (1) We assume, based on the crustal structure of the Barents Sea, that the shelf was formed by rifting of the platform (cratonic) lithosphere (Artemieva & Shulgin, 2019). Therefore, the lithosphere thickness should be similar to continental extensional areas. (2) Our choice does not contradict regional tomography models for the Arctic region, which remain highly controversial, in particular, because of a very thick sedimentary cover (cf. Lebedev et al., 2018). In particular, a regional tomography model (Levshin et al., 2007) may be interpreted in terms of a 80–130-km-thick lithosphere beneath the Barents Sea, if defined by a >2.5% V_s anomaly.

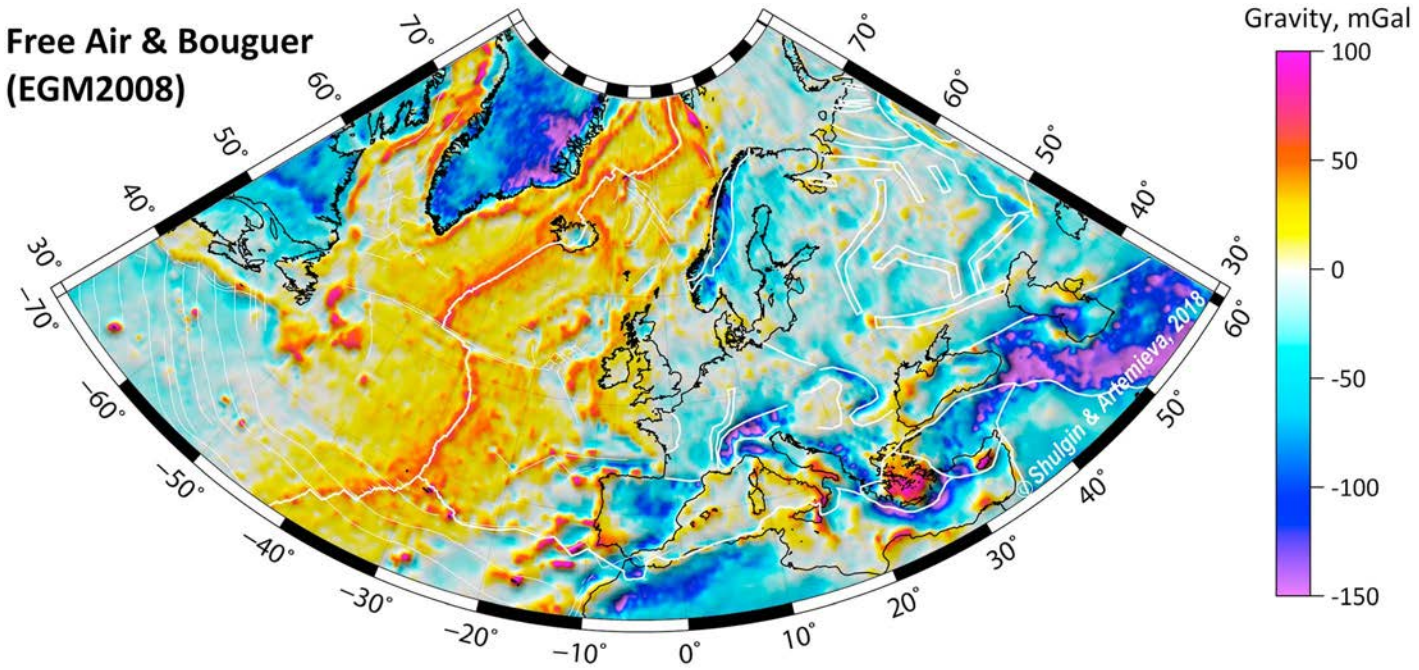

Figure 6. Gravity anomalies (free air for oceans and Bouguer for continents assuming reduction density of 2.67 g/cm^3) based on the EGM2008 model (Pavlis et al., 2012).

For the oceans, the depth to the LAB is calculated using the half-space cooling (HSC) model, based on the age of the seafloor. For young oceans around the mid-ocean ridge (MOR), we use the minimum value of 40 km for the LAB depth. This assumption may not be fully correct for the anomalous region around Iceland, and we address it in the discussion section. We do not use seismic tomography models to constrain the LAB depth due to a significant controversy between the existing models which cover the entire region (Schaeffer & Lebedev, 2013).

Figure 5a shows thickness of the LM calculated as the difference between the LAB and the Moho depths. The LAB depth controls the lithosphere geotherms, which are needed to separate thermal and compositional components of mantle gravity and density anomalies. Average temperature in the LM is the arithmetic mean between the LAB and Moho temperatures. We assume that temperature at the LAB is 1300 °C. For the continental part, the Moho temperatures are based on the TC1 model. For oceans, we use a linear temperature gradient in the lithosphere and assume thermal conductivity of 2.5 $W{\cdot}m^{-1}{\cdot}K^{-1}$ for the crust and 4.0 $W{\cdot}m^{-1}{\cdot}K^{-1}$ for the LM. It is counter-intuitive that oceans have a colder LM than SCLM (Figure 5b). The reason is a thin oceanic crust, and therefore low Moho temperatures. The Iceland region has an extreme average temperature in the LM (close to 1300 °C) because of a thick crust (25–30 km) and a shallow LAB (fixed at 40 km since the region is at the MOR).

3. Method

3.1. Gravity Effects of Remote Zones and Sphericity

Free air gravity anomalies in the ocean and Bouguer gravity anomalies on the continent (for reduction density of 2.67 g/cm^3) are based on the EGM2008 global gravity model (Pavlis et al., 2012) resampled with 0.5° to match the resolution of the crustal model (Figure 6). The gravity modeling is based on the 3-D gravity code "Tesseroids" (Uieda et al., 2016). It computes the gravity response of spherical tesseroids at close proximity to the sea level (+10 m elevation), therefore including the effects of both the sphericity (important for large regions and deep-seated gravity anomalies) and the remote zones. We use tesseroids with the sides of 0.5°, centered at grid nodes of the EUNAseis model, and down to the depth of 400 km. The 3-D gravitational effect is computed for the 10 neighboring crustal columns in each direction; that is, we took into account gravity effects within a 5° radius for each surface point. Doubling the radius leads to a significant increase

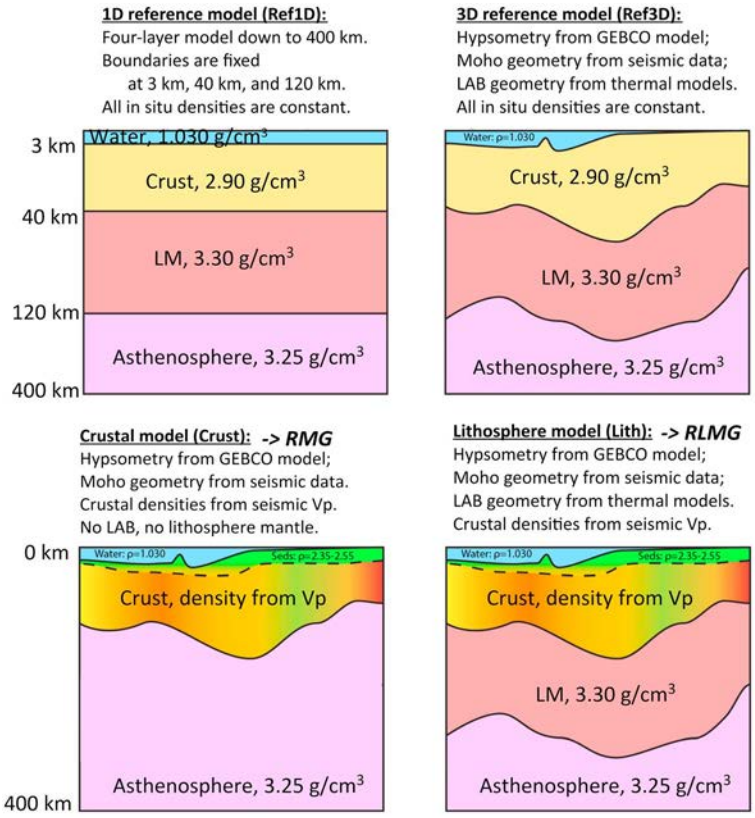

Figure 7. Reference models used in gravity modeling. See details in text. LAB = lithosphere-asthenosphere boundary; RLMG = residual lithosphere mantle gravity anomalies; RMG = residual upper mantle gravity anomalies.

in the computation time without notable change in the results, similar to conclusions of other studies (e.g., Szwillus et al., 2016).

The calculation includes computing gravitational anomalies down to the mantle transition zone, including the gravitational effects of the intracrustal boundaries (including sediments), the Moho topography, and the geometry of the LAB. These gravitational effects are particularly important in regions with a large gradient in the crustal and upper mantle density structure, where the difference between the full 3-D solution and the Bouguer thin (infinite) plate approximation (without an account for the gravity effects of sphericity and remote zones) can reach up to ±100 mGal (Figure S2).

3.2. Gravity Effects of Intralithospheric Boundaries and Crustal Structure

We first analyze the gravitational effects of crustal density heterogeneity and of the Moho and at the LAB topographies. Four different gravity models, which introduce a step-by-step complexity into the reference model, are computed for a comparison: 1-D reference model (Ref1D), 3-D reference model (Ref3D), 3-D crustal model (Crust), and 3-D lithosphere model (Lith; Figure 7).

1. The 1-D reference model is a simple four-layer model with fixed depth to the Moho and LAB boundaries and constant densities in each layer. It consists of a 3-km-thick water layer with $\rho = 1.03$ g/cm^3, 37-km-thick crustal layer with $\rho = 2.90$ g/cm^3, 80-km-thick LM with in situ density $\rho = 3.30$ g/cm^3, and asthenosphere down to a 400-km depth with in situ density $\rho = 3.25$ g/cm^3. Densities in the two mantle layers correspond to SPT peridotite density of 3.40 g/cm^3 (at Standard P-T conditions at $P = 1$ atm and $T = 20$ °C) for thermal expansion coefficient $\alpha = 3.5 \cdot 10^{-5}$ $1/K$ and mantle temperatures of 900 and 1300 °C, respectively.
2. The 3-D reference model (Ref3D) has the same four layers with the same constant densities as (Ref1D), but takes into account the geometry of the seafloor (based on the GEBCO model (GEBCO: General Bathymetric Chart of the Oceans, 2010)), the Moho (based on the EUNAseis database), and the LAB depth (based on the TC1 model for continents and half-space cooling model for oceans, Table 1).

Therefore, the difference between the gravitational effects of (Ref3D) and (Ref1D) quantifies the gravitational effect of the three major boundaries (bathymetry, the Moho, and the LAB). This difference is, in general, in the range from −200 mGal to +200 mGal and with larger values locally (Figure S3a).

3. The 3-D full model (Lith) differs from (Ref3D) by including the detailed information on the lateral variations in crustal densities (calculated layer by layer from the V_p velocities in the EUNAseis crustal model), and the gravitational effect of each crustal layer is calculated separately. Densities of the LM and asthenosphere are constant and the same as in the reference models (Ref1D) and (Ref3D; Figure 7). Therefore, the difference between the gravitational effects of the (Lith) and (Ref3D) models quantifies the gravitational effect of crustal density heterogeneity, which is, in general, also in the range from −200 mGal to +200 mGal (Figure S3b).
4. Finally, the (Crust) reference model differs from the (Lith) model by excluding the LAB boundary (we assign density of the LM the same value as the asthenosphere density in other reference models; Figure 7). Therefore, this model constrains gravity anomalies in the upper mantle in the layer between the Moho and the mantle transition zone, without the assumption that all density heterogeneity should reside in the lithospheric model.

3.3. Residual Gravity Anomalies: RLMG and RMG

To calculate density anomalies in the LM, we first compute residual gravity anomalies produced by density heterogeneity within the lithosphere mantle (between the Moho and the LAB), residual lithosphere mantle gravity anomalies (RLMG). They are calculated as the difference between the EGM2008 gravity anomalies (free air anomalies for oceans and Bouguer anomalies for continents) and the calculated gravity effect of the (Lith) model with respect to the (Ref1D) model:

$$\mathrm{RLMG} = \mathrm{EGM2008} - \mathrm{GLith} + \mathrm{GRef1D}. \tag{2}$$

Since reference models are to some extent arbitrary (and given the tectonic complexity of the region, it clearly cannot be matched by the same lithosphere model everywhere), the choice of a different reference model will cause a systematic shift of RLMG by a constant value. Here a static shift of −275 mGal is used to center the *G(Lith) – G(Ref1D)* anomalies at zero (Figure S3c). The resulting map of the residual LM gravity anomalies is shown in Figure 8a. Later the RLMG anomalies are used to calculate density anomalies in the LM, and we ensure that a systematic shift of RLMG is justified by comparing the calculated LM density with experimental data on mantle-derived peridotites. In particular, SPT density values of 3.33–3.35 g/cm^3 are typical of both oceanic mantle (Afonso et al., 2007) and mantle-derived cratonic peridotites (Gaul et al., 2000). They correspond to in situ LM density $\rho_0 = 3.24$ g/cm^3 for an average LM temperature of 800–950 °C, and we use these values as a reference frame for the calculated LM density.

Residual mantle gravity (RMG) anomalies are calculated as the difference between the EGM2008 gravity anomalies (Figure 6) and the calculated gravity effect of the (Crust) model with respect to the (Ref1D) model:

$$\mathrm{RMG} = \mathrm{EGM2008} - \mathrm{GCrust} + \mathrm{GRef1D}, \tag{3}$$

with a static shift of −160 mGal to center *G(Crust) – G(Ref1D)* anomalies at zero (Figure S3d; that is our assumption on the LAB boundary in the (Lith) model shifts the average gravitational effect by 115 mGal for the whole region). The resulting map of the residual gravity anomalies is shown in Figure 8b. This model does not include any assumptions on the thickness of the anomalous mantle layer and therefore is suitable for discussing a possible presence of deep-rooted temperature anomalies in the North Atlantic region, such as may be expected beneath Iceland.

We emphasize again that both RLMG and RMG anomalies are not in absolute, but in relative values because they depend on the choice of the reference model (Ref1D), and the choice of a different model will shift all values systematically by a constant. Therefore, the results are best suited for a comparison of different regions because such comparison removes the effect of the reference model. To circumvent the effect of the reference model, we also perform other types of the analysis, including the calculation of LM density.

3.4. Lithosphere Mantle Density

LM density can be calculated from the RLMG anomalies (Figure 7). Average in situ LM density (in g/cm^3) at each grid point can be estimated from the modified Bouguer approximation as

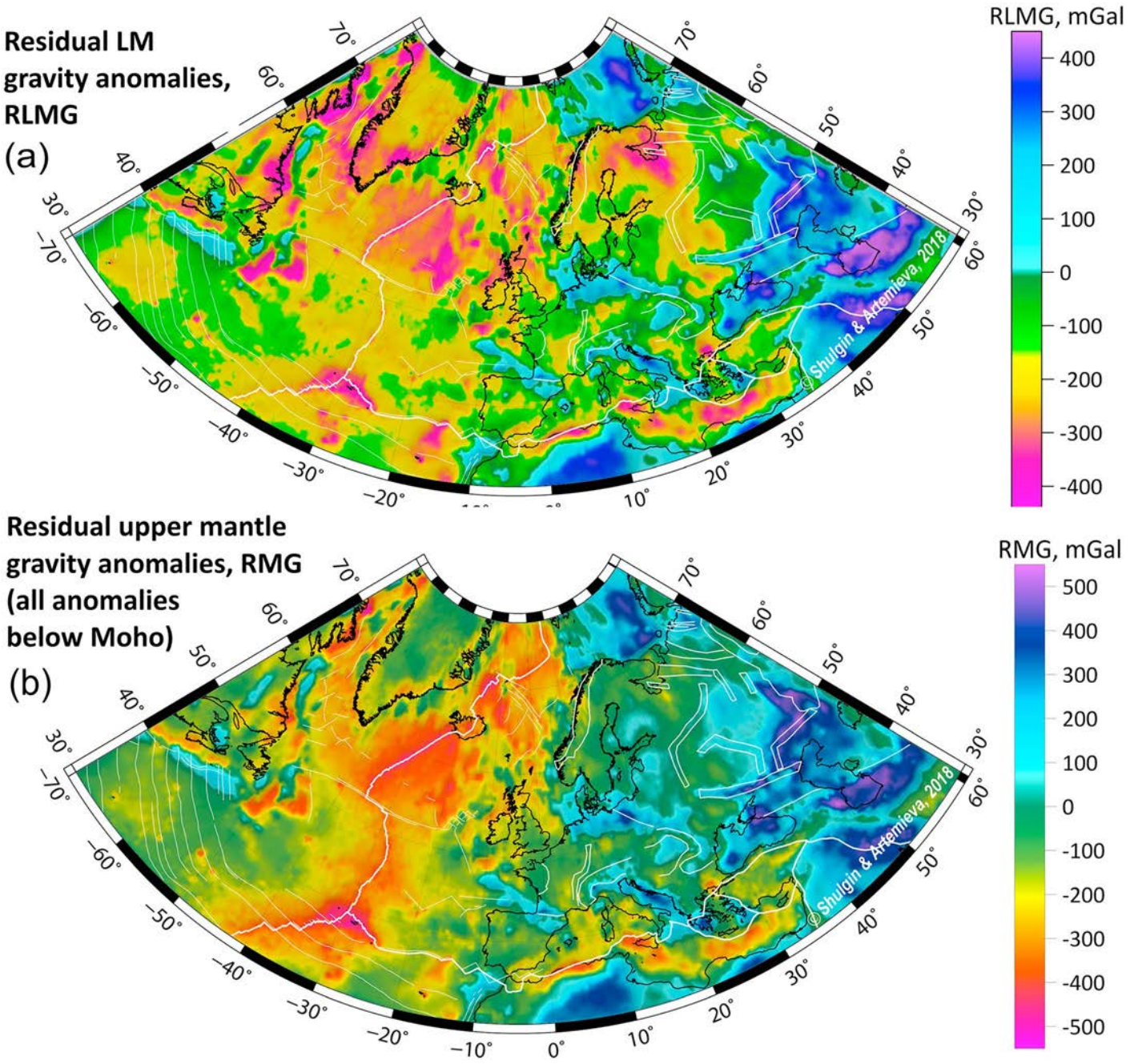

Figure 8. (a) Residual lithospheric mantle gravity anomalies (RLMG) calculated by subtracting the gravitational effect of the lithosphere model (Lith; Figure 7) from the observed gravity field (Figure 6). RLMG variations are caused by density anomalies in LM (between the Moho and the LAB). (b) Residual upper mantle gravity anomalies (RMG) calculated by subtracting the gravitational effect of the crustal model (Crust; Figure 7) from the observed gravity field (Figure 6). RMG variations are assumed to be caused by density anomalies between the Moho and the mantle transition zone. LM = lithospheric mantle; LAB = lithosphere-asthenosphere boundary.

$$\rho = \frac{\Delta g \cdot C}{41.93 \cdot H_{LM}} + \rho_0, \tag{4}$$

where Δg are RLMG anomalies (in mGal), H_{LM} the thickness of the LM (in km), and C is geometrical factor that takes into account the 3-D gravitational effect (ignored in the Bouguer approximation) of density anomalies from the neighboring cells. Geometrical factor quantifies the fraction of the total gravitational effect of LM density anomalies that comes from the LM located directly below a given cell, and

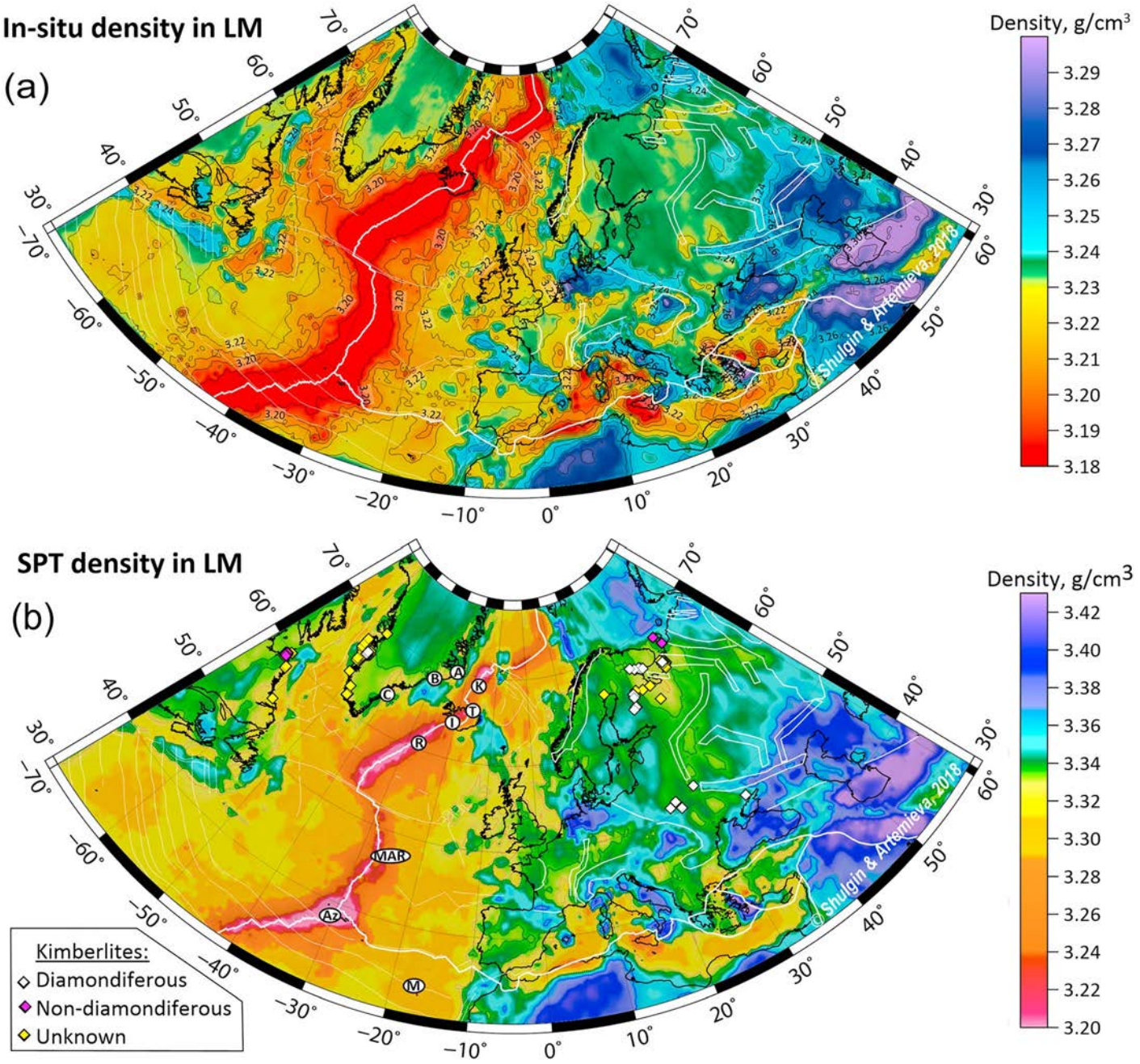

Figure 9. (a) In-situ density in lithospheric mantle (LM). Our results may overestimate the amplitude of the anomalies along the MOR. Low density along the MOR are due to a small thickness of lithosphere mantle, which is limited by the lithosphere-asthenosphere boundary depth of 40 km, while mantle melting responsible for mid-oceanic ridge basalt generation takes place at greater depths. (b) Density in LM with the temperature effect removed. SPT = standard *P-T* conditions at room pressure and temperature. Kimberlite provinces are shown by diamonds. Abbreviations refer to locations with geochemical data on mantle composition (see Figure 14): A, B, C = locations along the East Greenland coast, Az = Azores, M =Madeira, MAR = mid-Atlantic ridge, R = Reykjanes ridge, K= Kolbeinsey ridge, I = SW Iceland, T = Theistareykir; MOR = mid-ocean ridge.

takes into account crustal geometry, the LAB depth, the latitude correction, and the Earth's sphericity. For each grid point, the gravitational effect of the LM density anomalies is calculated within a 180-km radius, and the computed geometrical factor shows the ratio between gravitational effects of the LM anomalies computed in the Bouguer plate approximation and for 3-D gravity calculation with tesseroids (Figure S4).

The calculated in situ density provides the value averaged over the layer from the Moho to the LAB (Figure 9a). These values can directly compared to other remote geophysical models (e.g., seismic tomography), which also sample mantle at in situ conditions. Here we note that the in situ LM density model and seismic tomography models cannot be expected to be well correlated. (1) The density model shows the anomalies integrated over the thickness of the LM layer, while velocity models (e.g,. Legendre et al., 2012) provide depth slices. (2) In situ density anomalies reflect variations in temperature, melt, and composition. Seismic velocities are controlled by a much broader spectrum of parameters, which includes grain size variations and anisotropy, to which density is insensitive. (3) Temperature variations have different effects on density and V_s (Schutt & Lesher, 2006): A temperature anomaly of 50 °C will produce a 0.5% change in V_s but only 0.2% change in density (Deschamps et al., 2002). (4) The presence of trace fractions of a fluid phase (melt and water, as imaged by seismic attenuation in the European and North Atlantic mantle (Zhu et al., 2013) has little effect on density, but it leads to a sharp drop in seismic velocities. As a result, we do not expect a strong correlation between seismic velocities and densities in the upper mantle, in contrast to model assumptions used in some gravity studies (Kaban et al., 2016).

To compare the results with petrological data, the LM density values should be recalculated to the SPT conditions (room pressure and temperature) by removing the gravitational effect of thermal expansion. Although compressibility also effects mantle density (Simon & Podladchikov, 2008), the effect can be neglected because the calculated LM density is integrated over the layer at similar depths, from the Moho to the LAB. The correction for lateral temperature variations in LM is based on average temperature T in the LM at each grid point (Figure 5b) and SPT density is determined as

$$\rho_{\mathrm{SPT}} = \rho_{\mathrm{insitu}}(1 + \alpha \cdot T), \tag{5}$$

where $\alpha = 3.5 \cdot 10^{-5}$ 1/K. The resulting SPT density variations in the LM are shown in Figure 9b.

3.5. Uncertainty in Lithosphere Density

We use the calculated in situ LM density and the earlier calculated gravitational effect of the crust to recover the gravity field. The misfit between the recovered gravity field and EGM2008 (Figure S5a) is close to zero for most of the region, with significant deviations (~100 mGal) in deep (>15 km) sedimentary basins, where 3-D gravitational effects are particularly important due to a large density contrast between the sedimentary cover and the mantle. Regions with a large gravity misfit (the Central and Eastern Mediterranean, the Black Sea, the Caucasus, the Zagros orogen, Anatolia, and the East Barents Sea) also correspond to areas where the presence of slabs in the mantle is expected. Since these slabs are located below the LAB, their gravitational effect cannot be included into our gravity recovery calculation, therefore leading to large misfit values. Therefore, the misfit provides a measure of dynamic (mantle) contribution to the topography.

We next use the misfit values (Figure S5a) to calculate the uncertainty of lithosphere density (Figure S5b), which includes errors in crustal density estimates (Figure 4a) and in the calculation of LM density (Figure 9a). For the cratonic and western Europe and for most of the North Atlantic ocean the uncertainty is <0.005 g/cm^3. In regions with a large gravity misfit and a poorly known crustal structure (the southeastern part of the study region and the East Barents Sea), the uncertainty in the average lithosphere density (crust and LM) is typically 0.010–0.030 g/cm^3 with local anomalies up to ~0.050 g/cm^3. We therefore conclude that, overall, our lithosphere density model is well constrained.

4. Overview of Results

Our major results are RLMG anomalies (Figure 8a) and lithosphere mantle density anomalies at in situ and SPT conditions (Figure 9ab). All these types of anomalies are assumed to originate within the LM, between the Moho and the LAB. This assumption, which explicitly follows from the procedure used to calculate the RLMG anomalies and LM density, is particularly important for the anomalous region around Iceland, where the anomalous mantle may have a deep origin, much below the LAB depth. The thickness of the LM layer is laterally variable (Figure 5a), and the results depend on its thickness.

To address this problem we examine separately RMG anomalies calculated by subtraction of the crustal gravity signal from the observed gravity (Figure 8b). The depth distribution of these anomalies is unknown but can be indirectly assessed from their wavelength, since the maximum depth of a density anomaly is

tightly related the width of the gravity anomaly that it produces. In particular, for simple geometries, the depth to the anomaly center is proportional to ~0.65 of the anomaly width in case of a sphere and to ~0.5 of its width in case of a horizontal cylinder. A 300- to 400-km-wide and ~2,000-km-long RMG anomaly of ~ +200 mGal along the Trans-European Suture zone (TESZ) may be, roughly interpreted as caused by a cylindrical high-density body at ~150- to 200-km depth (Figure 8b). We address this topic in sections 5 and 6.

A comparison of in situ mantle density (Figure 9a) with recent seismic tomography models (Schaeffer & Lebedev, 2013) at a 100-km depth (Figure S6) shows an agreement in some large-scale features, and significant disagreement in many details (as discussed in section 3.4, we do not expect a strong correlation between mantle densities and velocities). In oceans, both models agree in resolving a low-V_s, low-density anomaly along the mid-Atlantic ridge (MAR) with the strongest anomaly centered around the Azores hot spot and the Kolbeinsey and Reykjanes ridges south and north of Iceland. Both models resolve an increase in V_s and in situ density from the MAR toward the old ocean, which reflects thermal cooling of oceanic lithosphere with age. On continents, the tomography model largely images the difference between the fast cratonic LM and the slow Phanerozoic LM and supports a continental origin of the Barents Sea lithosphere (Dore, 1995). In situ densities show a more complex pattern of the anomalies, with prominent high-density anomalies in the SE part of the region around the Caspian Sea. We discuss a possible origin of these anomalies in the next sections.

5. Density of Subcontinental Lithosphere Mantle (SCLM)

5.1. Origin of SCLM Density Heterogeneity

The next section focuses on SPT density anomalies in LM (Figure 9b), which reflect compositional variations (including fluids and melt). SPT density values may be directly compared to geochemical and laboratory data on rock composition and physical properties. Before discussing the results, we summarize the mechanisms which may cause density heterogeneity of SCLM.

5.1.1. Age Dependence

SCLM is the chemical and thermal boundary layer formed as residue after melt extraction from the convective mantle (Carlson et al., 2005). Secular cooling of the Earth leads to formation of SCLM under changing mantle temperature and melting conditions, resulting in secular variations in its major element composition and in bulk properties (elastic moduli, seismic velocities, and densities). High mantle temperatures on the early Earth produced the unique (Fe-poor) composition of the cratonic LM (Carlson et al., 2005) with low SPT density and high seismic velocities (Lee, 2003). Global studies of kimberlite-hosted mantle-derived xenoliths show that typical SPT densities range from 3.30–3.33 g/cm^3 for the Archean SCLM to 3.34–3.36 g/cm^3 for the Proterozoic SCLM, and 3.37–3.39 g/cm^3 for the Phanerozoic SCLM (Gaul et al., 2000). Note that kimberlite sampling of the cratonic mantle is non-uniform and apparently biased, so that the pristine Archean mantle with the most depleted composition is not sampled by kimberlite-hosted peridotites and its physical properties (e.g., density) are not constrained by geochemical data (Artemieva, 2009; Artemieva et al., 2019; Artemieva & Vinnik, 2016). Therefore, the range of expected SPT density of SCLM is from 3.30 to 3.39 g/cm^3.

5.1.2. Compositional Modification

The planetary cooling is irreversible; therefore, the compositional trend for SCLM is also irreversible; it means that once a highly depleted ancient SCLM is destroyed, it cannot be recreated, and any modification leads to its densification. This conclusion is supported by a strong heterogeneity in SCLM density (from 3.28–3.30 g/cm^3 to 3.40 g/cm^3) for the cratons of the Archean-early Proterozoic age (Artemieva & Vinnik, 2016; Cherepanova & Artemieva, 2015). Chemical densification of the continental LM may take place through metamorphic reactions or through mantle metasomatism in the cratonic settings.

Metasomatism of depleted cratonic LM, usually associated with basaltic magmatism (e.g., Griffin et al., 2005; Howarth et al., 2014), decreases the Mg/Fe ratio, increases LM density and decreases seismic velocities (Jordan, 1981; Lee, 2003). As a result, density of depleted SCLM may increase to the values typical of fertile adiabatic LM (Figure 10a).

Metamorphic reactions may also cause LM densification. The most important one is eclogitization because of the abundance of eclogite in the cratonic LM (Barth et al., 2002; Kopylova et al., 2016; Shirey et al., 2001) and its high density (3.48–3.52 g/cm^3) as compared to mantle peridotite (Christensen & Mooney, 1995;

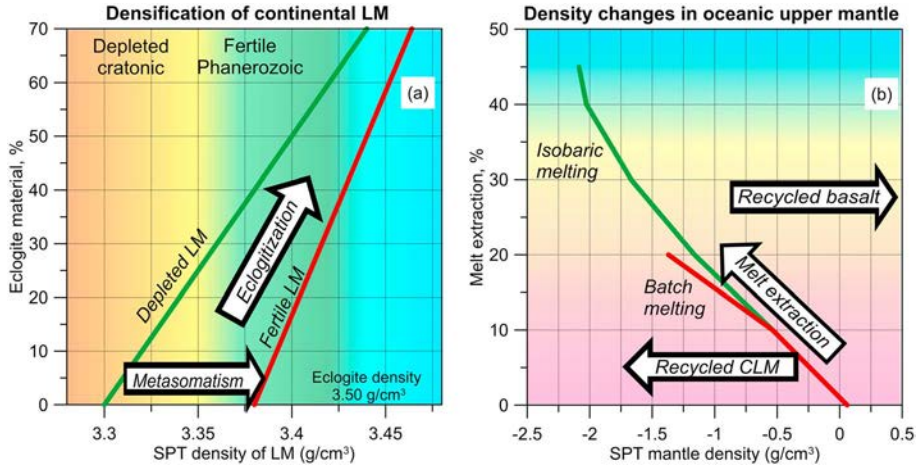

Figure 10. Trends in mantle density changes. (a) In continents, density of depleted cratonic mantle may increase by metasomatism (an addition of Fe-rich basaltic material) or by partial eclogitization. (b) In oceans, density of oceanic mantle depends on the amount of melt extraction by isobaric or batch melting (Afonso & Schutt, 2012). Recycling of depleted cratonic mantle and its mixing with the pyrolite mantle will reduce mantle density, while mixing of basaltic material (such as subducted oceanic crust) will have the opposite effect. SPT = standard P-T conditions at room pressure and temperature

Aoki & Takahashi, 2004; James et al., 2004; Figure 10a). Although eclogitization has been earlier proposed as subsidence mechanism for different deep basins of Eurasia and the Arctic shelf (Artyushkov, 2010), it has not been supported by geophysical observations. Our results (Figure 9) demonstrate the presence of a very dense mantle material beneath the Pannonian, Peri-Caspian, and the North German–Polish basins and thus provide the geophysical evidence that eclogitization may indeed be an important mechanism in formation of the super-deep intraplate basins, including the Barents Sea.

5.2. Precambrian Shields

Cratonic LM shows a strong heterogeneity in composition of the lithosphere mantle (Figure 9). Overall, the terranes of the East European craton with a low-density, depleted lithosphere mantle correlate with regions that have high V_s in the upper mantle at SPT conditions, calculated by removal of the effect of temperature heterogeneity from a seismic tomography model (Artemieva, 2009). There is no clear correlation between the geological age and mantle depletion in the Baltic shield, although in general the Archean blocks are more depleted than Proterozoic. The lowest densities of 3.32–3.33 g/cm^3 are typical of the Archean Kola-Karelia province of the Baltic shield, in agreement with geochemical data for ancient cratonic LM (e.g., Gaul et al., 2000), while LM density beneath the Archean-early Proterozoic Ukrainian shield and the Voronezh massif is slightly higher, ~3.33–3.34 g/cm^3. The Archean Lofoten block at the Norwegian coast in underlain by a low-density LM (3.32–3.33 g/cm^3), which extends inland beneath the northern dome of the Norwegian mountains.

There is no density difference between the Early Proterozoic (Svecofennian) and the Middle Proterozoic (Sveconorwegian) provinces of the Baltic shield. The Svecofennian province is dominated by values of around 3.34 g/cm^3, although the anomalies are patchy. LM of the north-western Finland has an increased density (~3.35 g/cm^3) and this high-density body extends beneath the Baltic Sea, providing support for the hypothesis that it may have been formed by Proterozoic rifting (Lahtinen et al., 2005). Alternatively, the high-density LM body may be associated with a 1.9-Ga paleosubduction imaged by seismic reflectors at a 50- to 80-km depth (BABEL Working Group, 1990), or with intensive mafic anorogenic magmatism in southern Fennoscandia at ~1.5 Ga (Vigneresse, 2005). This interpretation is consistent with the presence of a high-density (3.35–3.36 g/cm^3) LM body beneath the Baltic States, where a huge volume of anorogenic magmas was emplaced in Mesoproterozoic (Bogdanova et al., 2008).

In Greenland, low-density mantle (3.32–3.33 g/cm^3) dominates the southern, mostly Archean block, including the Isua greenstone belt of the Early Archean age. This low-density mantle continues in the

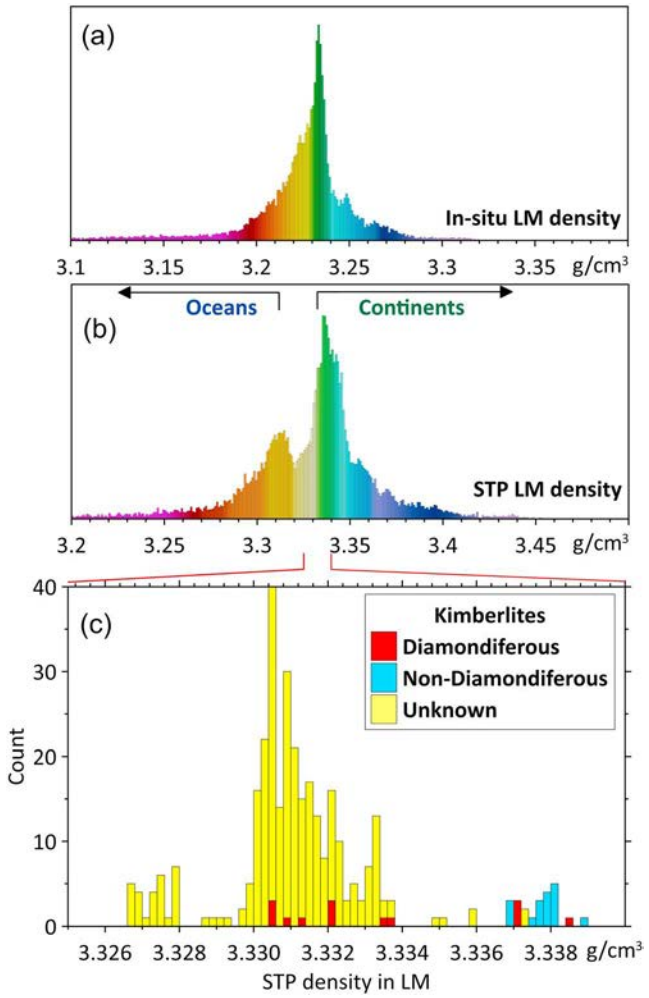

Figure 11. Distribution of lithospheric mantle (LM) densities (based on results in Figures 9a and 9b). (a) In situ LM densities; (b) temperature-corrected LM densities. The double-peak distribution reflects the difference between the oceanic and continental domains. (c) Temperature-corrected LM densities at the kimberlite provinces of Europe (based on results in Figure 9b). Note that all known nondiamondiferous kimberlites are restricted to LM with increased densities, while diamondiferous kimberlites are found in regions with a more depleted subcontinental lithospheric mantle. SPT = standard P-T conditions at room pressure and temperature; LM = lithospheric mantle.

Archean Nain province at the Atlantic coast of the Canadian shield. The central and northern Greenland and the Grenville province in Labrador have a denser LM with values around 3.34 g/cm^3, typical of Proterozoic mantle. Note that the crustal structure of Greenland is still poorly known and therefore the results for this region should be considered with caution. In central Greenland around the Summit station, where a high-resolution seismic data on the crustal structure exists (Kraft et al., 2019; Shulgin & Thybo, 2014), LM density increases to 3.35 g/cm^3 in the region where a ~10-km-thick high-velocity mafic layer is present in the lower crust (Figure 9). A narrow belt of a high-density mantle (3.36 g/cm^3) is present off-shore along the coast of East Greenland in the region affected by the North Atlantic LIP (Figure 1) and well covered by crustal-scale seismic profiles.

5.3. Kimberlites and SCLM Density

Abundant geochemical (Agashev et al., 2013; Aulbach et al., 2013; Doucet et al., 2014; Griffin et al., 2005; Hawkesworth et al., 1990; Howarth et al., 2014; Huang et al., 2014; Kargin et al., 2016; Peslier et al., 2010) and geophysical data (Artemieva, 2009; Artemieva et al., 2019; Artemieva & Vinnik, 2016; Cherepanova & Artemieva, 2015) from different cratons worldwide indicate that LM in kimberlite provinces is melt- and water-metasomatized. Our results indicate that the kimberlite provinces of Baltica, Greenland, and Labrador are all emplaced in regions with a low-dense (3.32–3.33 g/cm^3) LM (Figure 11), and nondiamondiferous kimberlites are clearly associated with a slightly denser mantle. Similar observation has earlier been reported for the Kaapvaal mantle, where statistically all kimberlite-rich regions have SPT mantle density of 3.32–3.33 g/cm^3, while kimberlite-poor regions have a higher density of ~3.35 g/cm^3 (Artemieva & Vinnik, 2016). In Kaapvaal this bimodal density distribution of LM density also correlates with the Moho sharpness; the absence of similar data for the East European craton does not allow for testing this conclusion for other cratons.

For the European-North Atlantic region, we interpret the absence of the LM with densities lower than in the kimberlite provinces as evidence that the region does not preserve any pristine, highly depleted Archean mantle, which has been metasomatically reworked by Proterozoic and Phanerozoic tectonomagmatic events (e.g., Beyer et al., 2006). Regional geochemical studies from the Karelian craton indicate that a highly depleted layer may be restricted to the upper section of the lithosphere mantle (Lehtonen et al., 2004).

5.4. Russian Platform, Intracratonic Basins, and Paleorifts

The Russian (East European) platform shows a strong variability in the LM density structure, similar to the cratons of Siberia (Cherepanova & Artemieva, 2015; Kaban et al., 2016) and southern Africa (Artemieva & Vinnik, 2016). In agreement with earlier studies (Artemieva, 2003, 2007), mantle density increases toward the southern parts of the platform, which have also experienced a fast subsidence and sedimentation since the Devonian. Lithosphere mantle of the Archean Volga-Uralia subcraton is denser (3.35–3.36 g/cm^3) than in other Archean cratons, suggesting its significant metasomatic reworking. Alternatively, it may include some eclogite as proposed in some formation models for the cratonic mantle (Barth et al., 2002; Schulze, 1989), and as observed in mantle-derived xenoliths from the cratonic mantle worldwide (Aulbach & Viljoen, 2015; Jacob et al., 1994; Kopylova et al., 2016; Schulze et al., 2000; Smart et al., 2012).

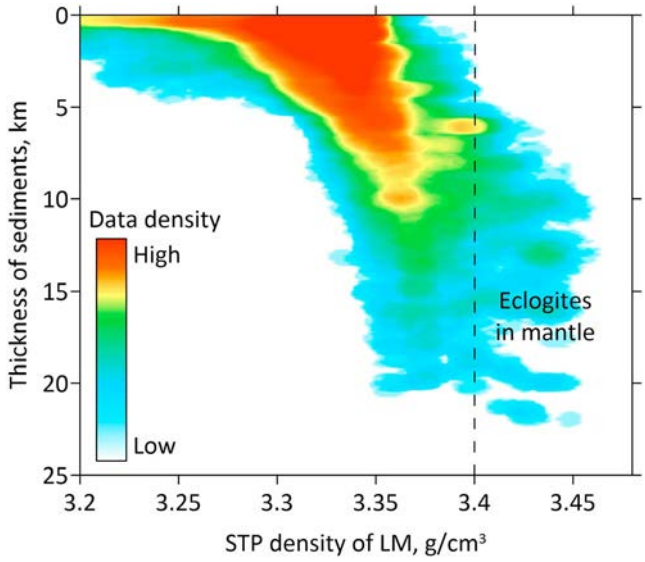

Figure 12. Data density plot showing thickness of sediments versus temperature-corrected lithospheric mantle (LM) density. The basin depth increases with the increase in LM density, as expected from isostasy. High LM density in superdeep basins requires partial eclogitization, which is therefore an important mechanism for deep basin formation.
STP = standard P-T conditions at room pressure and temperature.

Major Precambrian rifts of the East European craton have no signature in LM density, in a sharp contrast to the Paleozoic rifts. In particular, the Devonian Dnieper-Donets rift with 20–24 km of sediments has a very high-density LM, with a significant difference between the NW and SE parts where SPT mantle density is 3.35–3.36 g/cm^3 and 3.37–3.39 g/cm^3, respectively.

A strong correlation between mantle density and the depth of sedimentary basins (Figure 12) indicates that mantle eclogitization may an important mechanism in formation of the superdeep intraplate basins. The most prominent density anomalies in the cratonic mantle of the East European craton are associated with the Peri-Caspian depression which was formed in response to the Devonian rifting (Figure 9). High SPT mantle density (3.39–3.40 g/cm^3) suggests the presence of 10–20% of eclogite in a 70- to 100-km-thick layer below the Moho in case eclogitization took place in refertilized cratonic LM and up to 50% of eclogite in case the cratonic mantle still preserves a partially depleted composition (Figure 10a).

5.5. Arctic Shelf

We find a sharp distinction in the mantle density structure between the East and West Barents Sea shelves. The East Barents Sea has a high-density LM (3.38–3.39 g/cm^3), similar to the Peri-Caspian depression. These values do not exceed density of mantle peridotite and do not require the presence of a significant volume of eclogite in the mantle in case of a fertile LM composition. In this case, the density structure of the East Barents LM can be explained by a strong refertilization of the cratonic LM, such as associated with mantle delamination, similar to the mechanism proposed for the Mesozoic destruction of the North China craton (Gao et al., 2002). This process may possibly be followed by relamination (Kelemen & Behn, 2016), with an accretion of a new, fertile adiabatic mantle material to the shelf lithosphere.

Alternatively, mantle eclogitization may have also contributed to the East Barents Sea subsidence (Gac et al., 2014). In the east, the East Barents Sea is bordered by the orogen of the Novaya Zemlya archipelago, which is interpreted tectonically as a continuation of the Paleozoic Uralides orogen (Figure 1). Therefore, similar to the Uralides, one may expect the presence of a paleosubduction system beneath this part of the Arctic shelf. Water-rich conditions would facilitate metamorphic reactions, such as basalt/gabbro-eclogite transformation, given that even trace amounts of water may lead to rapid eclogitization (Austrheim et al., 1997). In case the LM has a major element composition similar to Proterozoic SCLM, the presence of 20–30% of eclogite cannot be ruled out (Figure 10a).

In contrast, the West Barents basin has density similar to Proterozoic cratons (~3.35 g/cm^3). Our results suggest significantly different subsidence history of the East and West Barents Sea and a possible presence of a major fault between the two contrasting basins of the European Arctic shelf. The contrasting structure of the East and West Barents Sea has also been identified in a regional tomography model (Levshin et al., 2007), but it is absent in a more recent model for the Arctics (Lebedev et al., 2018).

5.6. Craton to Noncraton Transition

Our modeling shows two unexpected results for the craton to noncraton transition in the upper mantle along the major tectonic and geological boundary in Europe, the Trans-European Suture Zone (TESZ).

1. We do not find a strong craton to noncraton transition in SPT mantle density across the TESZ, such as observed in seismic tomography models (Figure S6) and in an earlier gravity modeling based on an old map for the Moho depth and sedimentary cover with an unknown data coverage and no information on the inner velocity structure of the crust (Yegorova & Starostenko, 2002). We expect that the cratonic LM is depleted and low-dense, while the Phanerozoic mantle is fertile and high-dense; however we do not observe this in the results (Figure 9). Since the lithosphere is both thermal and chemical boundary layer, the explanation should be found in both temperature and compositional variations across the

TESZ. As on overall conclusion, one may argue that Jordan's isopycnicity hypothesis (Jordan, 1978, 1981) for the tectosphere structure (that is thermal and chemical effects on upper mantle density structure compensate each other) is roughly satisfied in Europe on the continent scale.

2. The lack of contrast in SPT density with a sharp contrast in seismic velocities between the cratonic and Phanerozoic Europe implies the following. Upper mantle seismic velocities are controlled by temperature variations to a greater extent than mantle density (e.g., Deschamps et al., 2002; see section 3.4), and therefore a pronounced difference between a low-velocity Phanerozoic mantle and a high-velocity cratonic mantle may reflect primarily a strong change in lithospheric geotherms across the TESZ (Artemieva, 2003, 2006). Temperature-corrected V_S velocities (at SPT conditions), which reflect changes in mantle composition and hydration, reveal a pronounced difference across the craton edges worldwide, including the TESZ (Artemieva, 2009). The lack of contrast in SPT density across the TESZ may indicate that significant parts of the cratonic LM are possibly essentially chemically reworked (as discussed above), while some parts of the Phanerozoic West European mantle may have depleted LM. We address this question below.
3. Our results suggest the presence of a high-density body in the upper mantle along the entire TESZ. This high-density belt with the RMG anomaly of ~ +200 mGal has a very regular width of ~300–400 km (Figure 8b), suggesting that the center of the (cylindrical) anomaly may be at a ~150- to 200-km depth, that is right below or at around the LAB. The high-density anomaly is right above the upper mantle low-V_S zone (−4.6% with respect to PREM), which also follows the TESZ from the Black Sea to southern Sweden (Zuilhuis & Nolet, 1994). The V_S anomaly, although not imaged in more recent regional tomographic models (Lebedev et al., 2018; Legendre et al., 2012; Zhu et al., 2013) was explained as the image of a highly hydrated subducting slab associated with closure of the Tornquist Ocean and collisional tectonics along the edge of the East European craton (Nolet & Zuilhuis, 1994). If this interpretation is correct, the high-density body imaged in our model may be the shallow part of the oceanic slab, which is not resolved in seismic tomography due to the counter play of composition and low temperature, on one side, and high water content, on the other side.

5.7. Variscan Massifs

Phanerozoic lithosphere of Western and Central Europe has been formed during the collapse of the Variscan orogen and includes the mosaics of Variscan (280–430 Ma) and Caledonian (400–500 Ma) terranes (Artemieva et al., 2006; Cloetingh et al., 2007). The presence of a strong seismic anisotropy in the lithosphere mantle of the Variscides is interpreted as evidence for Paleozoic subduction systems associated with the closure of the Rheic oceanic domains and the collision of the Gondwana and Laurasia continents (Plomerová et al., 1998). Lithosphere delamination concluded the Variscan orogeny (Menard & Molnar, 1988), leaving a thin crust with a nearly uniform thickness of 28–32 km (Figure 2c).

The Variscan massifs (the Bohemian, London–Brabant, Armorican, Iberian, and the Ardennes Massif) are recognized within the rest of Western Europe by the rheologically strong lithosphere (cf. Cloetingh et al., 2007). They include the lithosphere terranes of Proterozoic to Carboniferous ages, that experienced deformation, partial metamorphism and eclogitization (Franke, 1994), and voluminous granitoid emplacement between 370 and 280 Ma (Matte, 1986). Our results suggest that small blocks of the cratonic LM of the Gondwana and Laurasia continents could have survived during the Variscan orogeny and are now entrapped within the Phanerozoic lithosphere of Western and Central Europe. The Variscan massifs have a distinctly different lithospheric structure with cratonic-type LM densities, which range from 3.32–3.33 g/cm^3 in the Bohemian Massif to 3.33–3.34 g/cm^3 in other Variscan massifs.

Low mantle density (3.32–3.33 g/cm^3) beneath the French Massif Central and the Rhine Graben may be associated with the presence of a partially molten, low-density material at shallow depths, as suggested by regional tomography models (Zhu et al., 2012) and xenolith geothermobarometry (Werling & Altherr, 1997). TWe note that mantle-derived xenoliths constrain Palaeoproterozoic ages for some parts of the French Massif Central mantle (Wittig et al., 2006) and suggest that the massif has a relatively depleted LM in the northern part and fertile LM in the southern part (Downes et al., 2003; Uenver-Thiele et al., 2017). We cannot resolve the difference in SCLM density between the two parts of the massif, and our results may indicate the presence of some depleted cratonic mantle in the region.

5.8. Orogens

The Cenozoic orogens of Europe (Alps, Pyrenees, and Carpathians) are all associated with high-density LM anomalies, typically in the range 3.35–3.37 g/cm^3 (Figure 9). Regional tomography models with high-velocity bodies imaged down to 200- to 260-km depth suggest the presence of subducting slabs beneath these orogens (Hetenyi et al., 2018; Kastle et al., 2018; Lippitsch et al., 2003), and judging from the range of density values we do not expect slab eclogitization, which may occur locally where LM density increases to 3.39–3.40 g/cm^3. Our results agree with a recent study for Pyrenees where the absence of a high-density anomaly in the upper mantle was interpreted as lack of eclogitization of the subducted Iberian crust (Dufrechou et al., 2018).

Surprisingly, density of the upper mantle beneath the Paleozoic Urals is similar to the Cenozoic orogens, although significantly denser than beneath the Norwegian mountains. This difference possibly reflects the presence of some eclogitic material, such as in an eastward dipping high-velocity block with compressional velocities of ~8.7 km/s down to a 100-km depth (Ryberg et al., 1996). In agreement with our conclusion, an earlier gravity modeling suggests that most gravity anomalies in the Urals can be explained by a strong density heterogeneity within the island arc material of the Uralian crust, with a "normal" mantle density (Doring et al., 1997).

LM density structure of the Paleozoic Norwegian mountains is different. Our results suggest, in agreement with earlier conclusions (Artemieva, 2003), that the high topography of the Norwegian mountains, and especially of the northern dome, may have a strong compositional component. A similar conclusion was made for the southern dome of the Norwegian mountains (Maupin et al., 2013), where our results also show the presence of a relatively low-dense LM, ~3.33–3.34 g/cm^3. The calculated low LM density is also in agreement with geochemical studies of depleted mantle samples from southern Norway (Andersen & Sundvoll, 1995) and with the presence of a highly depleted SCLM beneath the Western Gneiss Region in southern Norway (Beyer et al., 2006). Yet high-resolution seismic data on the upper mantle structure beneath the southern Norway remains highly controversial (Maupin et al., 2013) and the origin of the high topography of the Norwegian mountains is still debated (Gabrielsen et al., 2010; Nielsen et al., 2012).

5.9. Basins

Major sedimentary basins (the Pannonian Basin, the North German Basin, the Po basin, the Peri-Caspian depression) all have an extremely high density LM (>3.39 g/cm^3). We explain these LM density anomalies by partial eclogitization of the lithosphere mantle which may require the presence of ~10–20% of eclogitic material in the LM of the sedimentary basins (Figures 10a and 12). In particular, thinning of the crystalline crust locally to 15–20 km in the South Caspian basin is sometimes interpreted as an evidence of oceanization (Allen, Jones, et al., 2002) and its subsidence is attributed to phase transitions in the lower crust (Artyushkov, 2007, 2010). Consequent sinking of a high-density material into the mantle may create high-density LM anomalies as observed in our model.

Our results indicate the presence of an extremely dense LM beneath the Black Sea and the Caspian Sea, and also beneath the Iranian plateau and the Zagros orogenic belt. A high LM density (3.40–3.47 g/cm^3), if correct, requires the presence of 20–70% of eclogite in the LM (Figure 10a). However, all of these regions have a poor seismic coverage on the crustal structure (Artemieva & Thybo, 2013), and therefore the results for these regions are poorly constrained.

6. Density of Oceanic Upper Mantle

6.1. Origin of OLM Density Heterogeneity

Oceanic lithosphere mantle (OLM) is formed as thermal boundary layer by cooling of lithospheric plates with age. It also forms chemical boundary layer as the product of mantle melting. Compositional structure of OLM is commonly expected to be more homogeneous than of SCLM, and the major factors controlling SPT density of oceanic upper mantle are the presence of partial melts associated with volcanic provinces, subducted oceanic crust, and continental fragments.

Mineralogy has a strong effect on mantle density (Schutt & Lesher, 2006) and a broad range of density values was reported for fertile adiabatic oceanic lithosphere mantle. Some of the largest SPT density values of

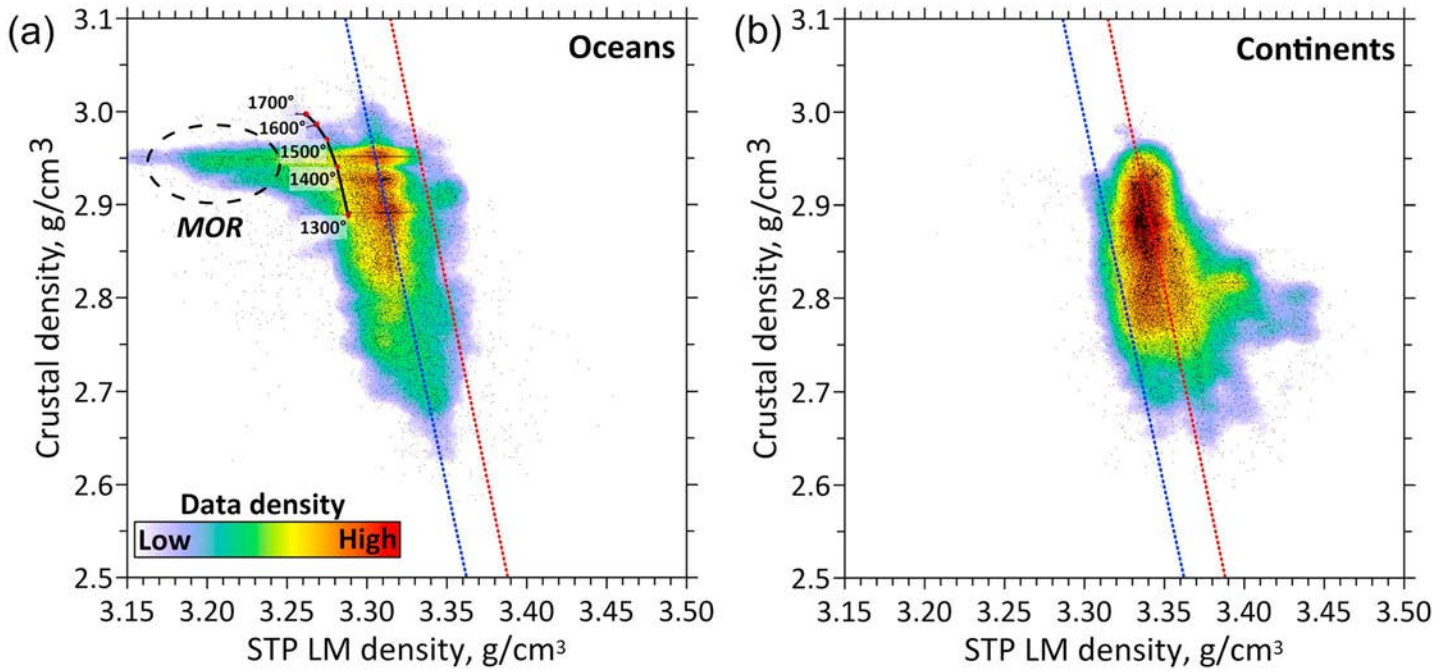

Figure 13. Crustal density (including sediments) in oceanic and continental domains (Figure 4a) as a function of lithospheric mantle (LM) density (Figure 9b). Oceans are distinguished from continents by the available sea floor age data. Oceanic domain may include some continental fragments. Crust and lithosphere mantle are both the products of mantle melting and their densities are expected to be related. Plots show color-coded data density; dots = data points; blue and red lines are trends for oceans and continents, respectively. Black line on the ocean plot = theoretical predictions for different mantle potential temperatures (numbers at the curve) (Korenaga, 2013). STP = standard *P-T* conditions at room pressure and temperature; MOR = mid-ocean ridge.

~3.38–3.39 g/cm^3 are based on calculations for pyrolite composition (Irifune, 1987; Poudjom Djomani et al., 2001). In situ density for average composition of oceanic MOR peridotite of 3.22 g/cm^3 (Simon et al., 2008) also yields SPT density of 3.38 g/cm^3 for average MOR peridotites. In contrast, some theoretical calculations favor low SPT density values for oceanic mantle, 3.325–3.336 g/cm^3 (Afonso et al., 2007; Afonso & Schutt, 2012; Cadio & Korenaga, 2014). Assuming that, similar to SCLM, oceanic upper mantle density structure is a linear melting function correlated with Mg#, Lee et al. (2004) calculated SPT density of oceanic mantle as 3.350 g/cm^3.

Mantle potential temperature at which OLM is formed and chemical heterogeneity of the melting source also control composition and density of oceanic lithosphere mantle. OLM generated at 1300 °C has density of ~3.29 g/cm^3 and an increase of mantle potential temperature to 1600 °C produces OLM with density of 3.27 g/cm^3 (Korenaga, 2013; Figure 13a). The presence of subducted oceanic crust in melting source reduces mantle temperatures required for melt generation in oceanic mantle (Brown & Lesher, 2014). The effect of melt depletion on density of garnet peridotite is also important: 25% partial melting at mid-ocean ridge will reduce mantle density by 1.9% (Jordan, 1979; O'Hara, 1975). For a 3.39 g/cm^3 SPT density of pyrolitic mantle, it implies SPT mantle density of 3.326 g/cm^3 at MOR. Recent modeling for batch and isobaric melting predicts a smaller (~1.0–1.5%) decrease in density of oceanic upper mantle at 25% partial melting (Afonso & Schutt, 2012; Figure 10b).

The presence of recycled LM (continental or Archean oceanic) within oceanic mantle is reported from geochemical studies of peridotites from hot spot-related ocean islands (e.g., Schaefer et al., 2002; Widom, 2002). These continental fragments can also significantly change OLM density. Ocean island peridotites from the Canary Islands with a high proportion of highly refractory, high Mg#, and low-density harzburgite have in situ density values as low as 3.20 g/cm^3 for a 100-km-thick mantle column at T ~ 1060 °C (Simon et al., 2008). These values correspond to SPT density of 3.32 g/cm^3. Some of the lowest values of 3.30 g/cm^3, similar to cratonic low-T peridotites, have been reported for basalt-depleted magmas in Iceland (O'Hara, 1975). Therefore, the range of expected SPT density of OLM is from 3.30 to 3.39 g/cm^3, that is the same as for

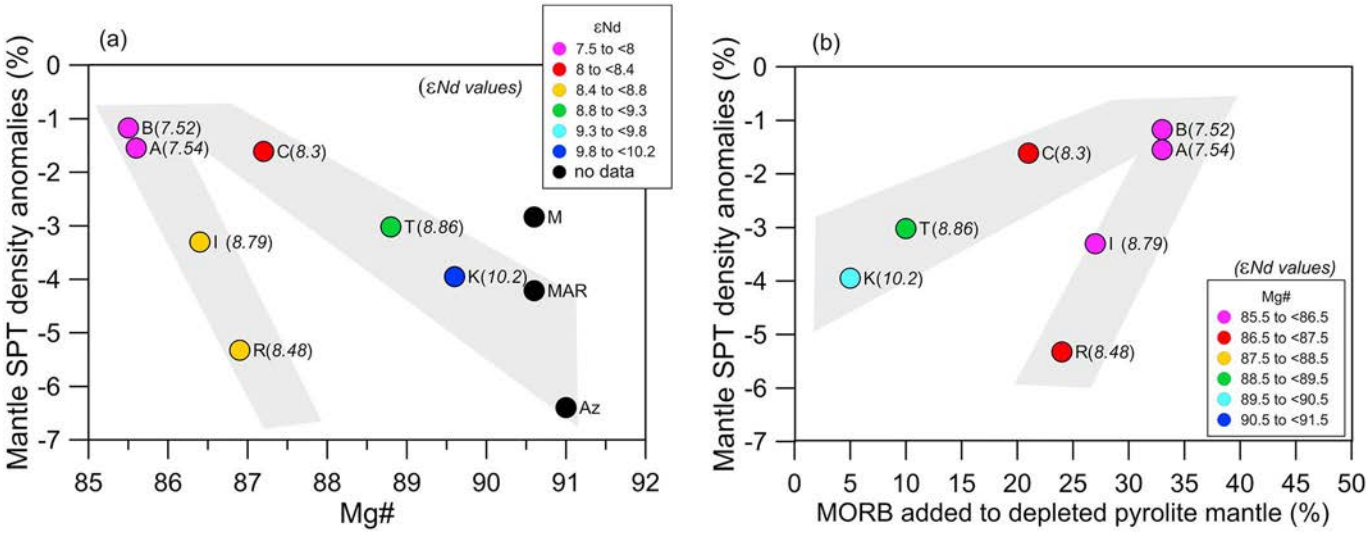

Figure 14. Mantle SPT density anomalies with respect to pyrolite mantle (Figure S8b) plotted versus geochemical data (letters refer to locations marked in Figure 9b; numbers in brackets – εNd values). **(a)** Mantle density decreases with Mg# increasing (that is with Fe-depletion). A strong density decrease at southern Iceland (I) and the Reykjanes Ridge (R) cannot be explained by chemical depletion alone and requires high mantle temperatures. High Mg# and low density mantle at and around the Azores (Az, MAR), at northern Iceland (Theistareykir) and at the Kolbeinsey Ridge (K) suggests the presence of some continental material. **(b)** The covariation of mantle density and the amount of basalt mixed with depleted pyrolite mantle (data of Korenaga and Kelemen (2000)). Mantle density increases when basalt mixes with the convective mantle. Locations A and B in East Greenland are within the Tertiary flood basalts, locations I and R are at the Mid-Atlantic Ridge. Geochemical data sources: Korenaga and Kelemen (2000) for the Iceland-Greenland region; Simon et al. (2008) for the North Atlantics hotspots (Azores and Madeira). STP = standard *P-T* conditions at room pressure and temperature; MORB= mid-oceanic ridge basalt.

SCLM. Our results, however, indicate that OLM densities in the North Atlantics are somewhat lower than in the European SCLM (Figure 13).

6.2. Chemical Heterogeneity of Oceanic Lithosphere Mantle (OLM)

We define the ocean mantle structure that follows the square-root-of-age pattern as "normal ocean." In situ mantle density anomalies (Figure 9a) reflect both temperature and compositional heterogeneity of oceanic upper mantle, while thermal effect associated with age-dependent ocean lithosphere cooling has been removed from the SPT mantle density variations (Figure 9b; see section 3).

South of the Charlie-Gibbs Fracture Zone (CGFZ), SPT densities show a uniform composition of the North Atlantic oceanic lithosphere mantle, with regional variations in OLM density mostly within 0.05–0.10 g/cm^3 around mean value of ~3.31 g/cm^3 (Figure 11b). This implies the density contrast between the oceanic lithosphere mantle and the convective mantle of about 0.07–0.08 g/cm^3 at SPT conditions and ~0.02–0.03 g/cm^3 at in situ conditions (Figure 9a), that is about twice less than commonly assumed in geodynamic modeling (e.g., Ficini et al., 2017; Schubert et al., 2001).

There is a sharp difference in the density structure of the OLM north and south of the CGFZ (Figures 9b and S7). The northern part is highly heterogeneous, and this heterogeneity reflects variations in both composition and chemistry. Major density anomalies are also associated with the Mid-Atlantic Ridge around the Azores hot spot and north and south of Iceland (the Kolbeinsey and Reykjanes Ridges). Importantly, in our modeling the OLM density anomalies (Figure 9b) are assumed to be restricted to the LM with the age-dependent LAB depth that follows the HSC ocean cooling model. We assume that along the MOR the LAB is at a 40-km depth, while mantle melting responsible for MORB generation takes place at greater depths. Therefore, our results overestimate the amplitude of the anomalies along the MOR (Figure S8). Furthermore, mantle temperature anomalies associated with hot spots may extend much deeper than the lithosphere base. We discuss this problem in detail in the next subsections.

Geochemical studies of oceanic peridotites from the North Atlantic region (Korenaga & Kelemen, 2000; Simon et al., 2008) allow for some speculations on the compositional origin of the OLM density heterogeneity. SPT density anomalies within the oceanic lithosphere mantle show inverse correlation with both Mg# and εNd in oceanic peridotites from East Greenland, MAR around Iceland, and the Azores (Figure 14). A general

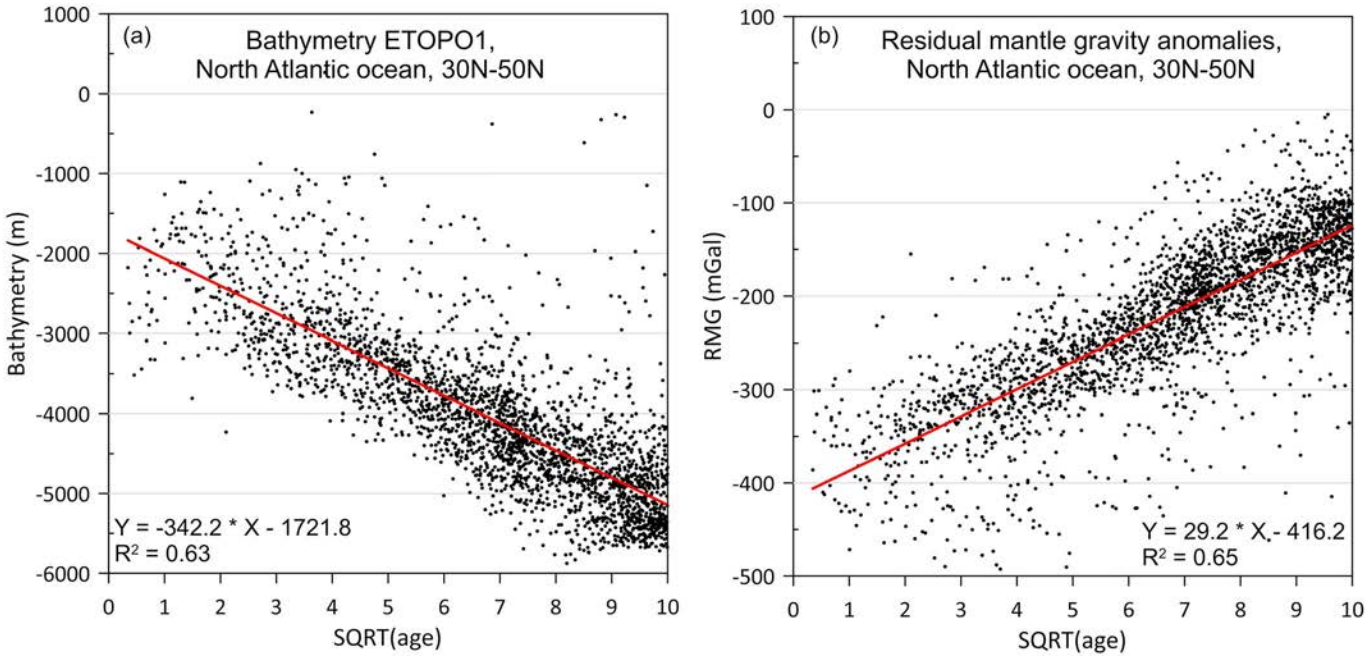

Figure 15. Age dependence of bathymetry (a) and residual mantle gravity (RMG) anomalies (b) in the southern part of the North Atlantic Ocean (south of the Charlie-Gibbs Fracture Zone). Red lines = best fit to data. This part of the North Atlantic Ocean follows the square root of age predictions of the half-space cooling model and is considered as "normal" ocean.

agreement of our results with the density-Mg# linear relationship (Lee et al., 2004) based on peridotite melting suggests that, at least in part, chemical heterogeneity of the North Atlantic oceanic mantle may be caused by a melting heterogeneity. Yet a low-density anomaly at southern Iceland and the Reykjanes Ridge (Figure 14a) is too strong to be explained by chemical depletion alone and it requires high temperatures and possibly a high-percentage melting in the upper mantle. Low mantle density at the Azores and the Kolbensey Ridge near the Jan Mayen continental terrane correlates with high Mg# and may indicate the presence of continental material in oceanic mantle, in agreement with geochemical data for the Azores (Widom, 2002).

In contrast, mixing of basalt with the convective mantle will increase mantle density. Such a situation may happen when basaltic oceanic crust subducts into the mantle. A comparison of mantle density anomalies with the mixing trend for basalt and convective pyrolite mantle (Korenaga & Kelemen, 2000) shows that the North Atlantic region around Iceland may have two different trends: One includes the ocean north of Iceland around the Jan Mayen block, and the other — East Greenland within the North Atlantic LIP and the region just south of Iceland (Figure 14b). A strong nonlinear correlation between Mg# and εNd in the North Atlantics around Iceland has earlier been interpreted by mixing between a recycled oceanic crust (formed at ~0.6 Ga by normal MORB) and depleted mantle (Korenaga & Kelemen, 2000), yet these authors are cautious in linking these basalts with the coeval Caledonian suture zone near the East Greenland margin. Our results suggest that oceanic basalts in the North Atlantics mantle around Iceland may play an important role in mantle density heterogeneity (Figure 14b). It is, however, outside the scope of the present study to discuss a possible origin of the observed chemical heterogeneity in the upper mantle of the North Atlantic Ocean.

6.3. Deviations of Mantle Structure From Half-Space Cooling (HSC) Model

To remove limitations related to the assumption that all density variations (of any origin) are restricted to the LM, we now focus on residual mantle gravity (RMG) anomalies. These anomalies (Figure 8b) are produced in the upper mantle layer between the Moho and the 400-km depth. As discussed above, the residual lithospheric mantle gravity (RLMG) and density structure of the North Atlantic Ocean south of the CGFZ is very uniform, implying that the upper mantle of this part of the ocean follows the HSC model. The analysis of bathymetry and RMG variations with age (Figure 15ab) further supports this conclusion. We therefore

consider the North Atlantic Ocean south of the CGFZ as "normal" ocean and use it as reference frame in our further analysis.

The map of anomalous bathymetry (Figure 16a), defined here as bathymetry from which the reference square-root-of-age trend is removed (Figure 15a, red line), shows that the entire North Atlantic Ocean north of the CGFZ is anomalous with the hypsometry 1–2 km more shallow than the ocean cooling predicts. South of the CGFZ deviations from the square-root-of-age trend are restricted to the ocean older than ~120 Ma (where some volcanic provinces are located) and to the Azores hot spot.

The anomalous ocean structure north of the CGFZ is even more striking for the Reduced RMG anomalies (Figure 16b), calculated by subtracting the reference square-root-of-age trend (Figure 15b, red line) from the RMG anomalies (Figure 8b). Importantly, the RMG and RLMG anomalies depend on the reference model (Figure 7), but the reduced RMG anomalies are independent of the reference model and are, therefore, in absolute values. Negative anomalies imply a low-density mantle, most likely associated with high mantle temperatures and the presence of a low-dense recycled lithosphere material, while positive anomalies indicate the presence of a high-density basaltic material in the mantle.

South of the CGFZ, all major anomalies are clearly associated with hot spots and volcanic islands. This includes the New England volcanic seamounts (−50–60 mGal), which are a part of the Meteor hot spot track in North America, the Azores (−150–240 mGal), the Madeira (−110–210 mGal), and the Canary Islands (~ −200 mGal, only a part of the region is covered by the study). The results also show a symmetric sublatitudinal anomaly (−30–40 mGal) across the Atlantic ocean at ~45°N, which has the pattern of a hot spot track, yet the authors are unaware of any hot spot track in this part of the North Atlantic Ocean. On the European side, this anomaly corresponds to the fracture zone that continues into the Bay of Biscay (Figure 1).

North of the CGFZ, the Reduced RMG anomalies are −60–80 mGal at the Reykjanes Basin and the Reykjanes Ridge and increase to −130–180 mGal toward the Rockall Plateau. Similar values are typical for the Labrador Sea. North of Iceland, the anomalies are −80–100 mGal at the Kolbeinsey Ridge with the largest anomaly of −150–200 mGal associated with the Jan Mayen block. The latter is usually interpreted as a continental fragment (Mosar et al., 2002), and therefore the Reduced RMG anomaly there includes both temperature and compositional components.

Positive Reduced RMG anomalies are restricted largely to the East Greenland margin (+40 + 160 mGal) and the Greenland-Iceland-Faroe Ridge (GIFR) across the Atlantic Ocean (0 + 50 mGal). The geodynamic origin of the GIFR, which has a ~25- to 30-km-thick crust remains enigmatic (Lundin & Dore, 2005; Parkin & White, 2008). Our results suggest that the deep structure of the GIFR is not fully symmetric: The major high-density anomaly is along the Greenland margin, where it is apparently associated with the North Atlantic LIP. We speculate that the anomaly is compositional in origin and, similar to continental mantle, may be caused by partial eclogitization of basaltic magmas associated with the LIP, facilitated by mantle hydration at the paleosubduction system (Schiffer et al., 2014). Therefore, the apparent absence of the anomaly at Iceland and along the GIFR may be caused by the counter-play of a negative low-density anomaly of thermal origin and a positive high-density anomaly of compositional origin. In case a low-density thermal anomaly around Iceland has the same magnitude as at the Reykjanes Ridge, the true high-density anomaly is ~ +200 mGal. This value is comparable to a very high density anomaly (+200 + 300 mGal) in the Bay of Biscay (Figure 16b) which appears really anomalous; its amplitude also suggests a chemical origin. Note that a similar RMG anomaly of ca +200 mGal in the Peri-Caspian region (Figure 8b) can be explained by the presence of ~10–20% of eclogitic material in the mantle (see section 5).

6.4. Mantle Temperature Beneath the MOR and Hot Spots

We speculate that a significant part of low-density Reduced RMG anomalies around the volcanic islands and hot spots in the North Atlantics is of thermal origin. Using the Bouguer plate approximation, one may estimate the amplitude of temperature anomaly ΔT, which causes a density decrease due to thermal expansion and produces a Reduced RMG anomaly ΔG:

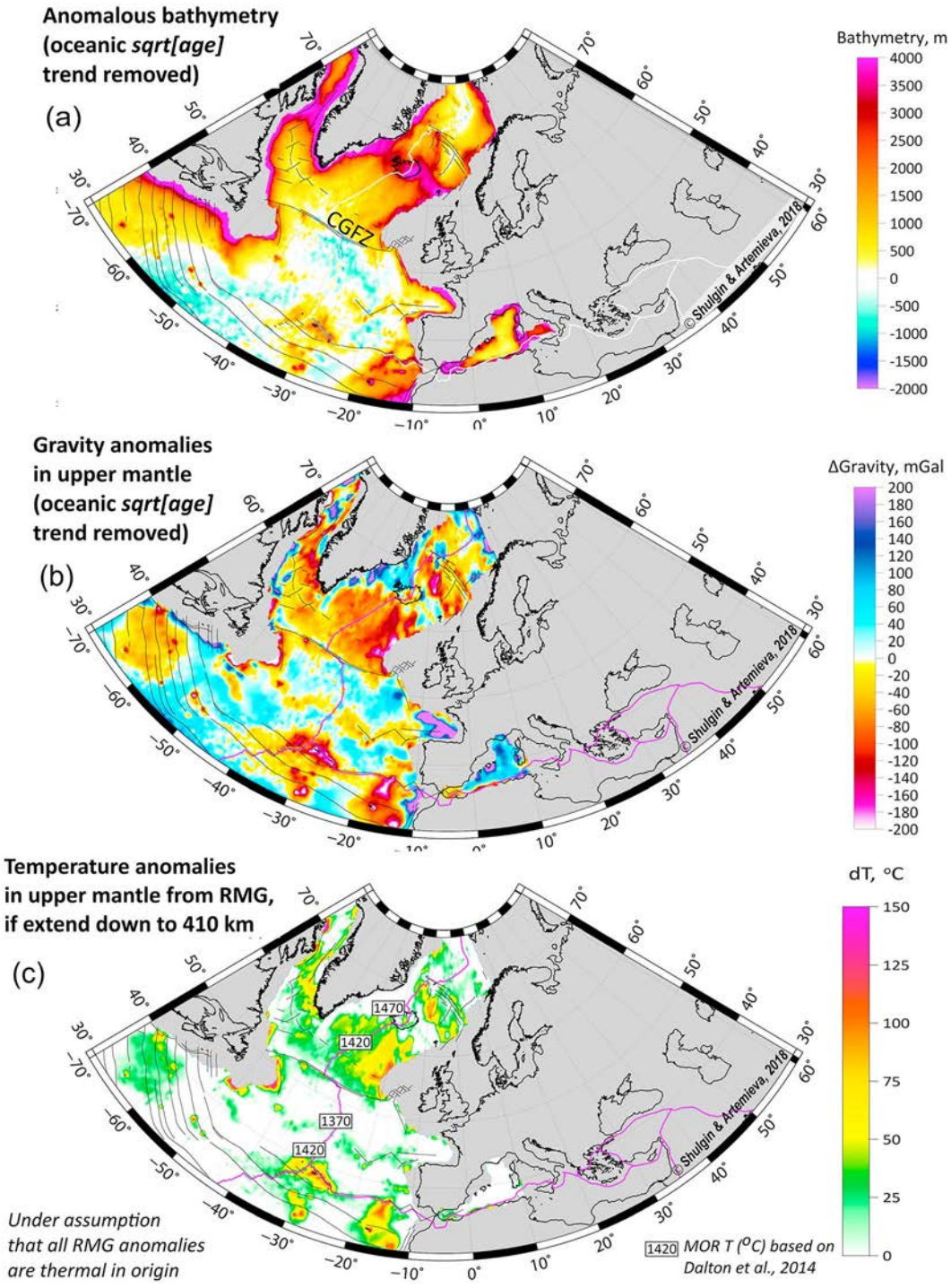

Figure 16. (a) Anomalous bathymetry in the North Atlantic Ocean calculated by subtracting the half-space cooling trend (Figure 15a) from the observed bathymetry. North of the Charlie-Gibbs Fracture Zone (CGFZ), the North Atlantics has on average 1–2 km positive anomalous bathymetry, which reaches 4 km at the Greenland-Faroe-Iceland ridge and in the Baffin Bay. (b) Reduced residual mantle gravity anomalies in the North Atlantics calculated by subtracting the half-space cooling trend (Figure 15b) from the RMG anomalies (Figure 8b). Strong negative anomalies north of the Charlie-Gibbs Fracture Zone require high mantle temperatures. The linear trend along ~ 45°N may be a trace of an unknown hot spot track. (c) Temperature anomalies in the upper mantle of the North Atlantic Ocean calculated from reduced RMG anomalies (b) under the following assumptions: (1) all gravity anomalies are thermal in origin; (2) their source is in the layer between the Moho and a 400-km depth. Numbers along the MOR = temperature estimates based on geochemical data (Dalton et al., 2014). The apparent absence of thermal anomaly at around Iceland and along the Greenland-Iceland-Faroe Ridge is due to a counter-play of a negative low-density anomaly of thermal origin possibly balanced by a positive high-density anomaly of compositional origin. RMG = Residual upper mantle gravity anomalies; MOR = mid-ocean ridge.

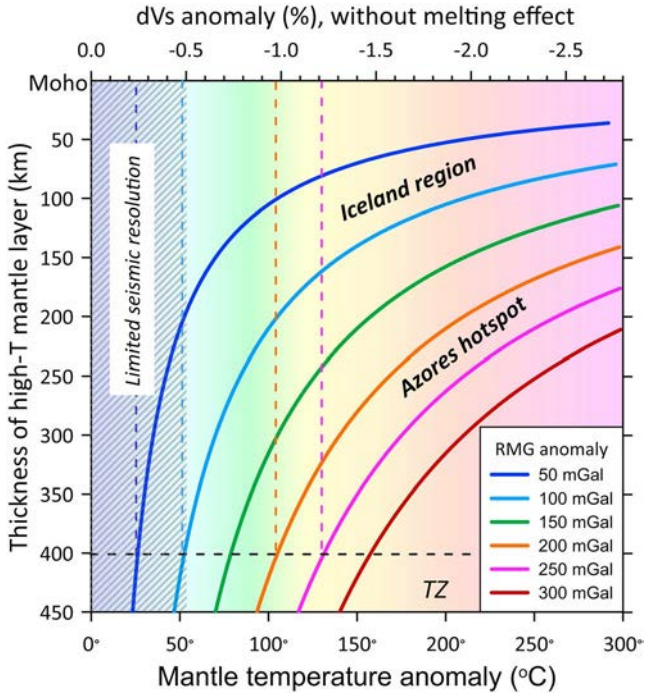

Figure 17. Mantle temperature anomaly versus thickness of a mantle layer with an elevated temperature. There is a trade-off between temperature anomaly and thickness of the heated layer in producing Residual upper mantle gravity (RMG) anomalies. For a given value of reduced RMG anomaly, the twofold increase of the layer thickness will result in more than double drop in the anomalous temperature. The reduced RMG anomaly beneath the Azores can be explained by a ~125 °C temperature anomaly distributed over a 400-km-thick layer, and such a temperature anomaly can be reliably resolved by seismic methods. In the Iceland region, the reduced RMG anomaly can be explained by a temperature anomaly of ca 110 °C if the heated layer extends 100 km below the Moho. However, if thermal anomaly extends down to a 410-km depth, its amplitude can be as small as 25 °C. Such a small increase in temperature will decrease V_S velocity by only ~0.2%, which is at the limit of resolution by seismic tomography.

$$\Delta G = 2\pi GH\rho(1 - \alpha\Delta T) \quad (6)$$

Here α is coefficient of thermal expansion, ρ is mantle density, H is thickness of the layer with a temperature anomaly, and G is the gravitational constant. In case a thermal anomaly extends through the entire upper mantle, from the mantle transition zone to the Moho, its amplitude in the region around Iceland is less than 50 °C, similar to mantle temperature anomaly at the New England seamounts (Figure 16c). Yet as discussed above, the absence of the anomaly at Iceland may be apparent due to the balancing effects of thermal and compositional anomalies. Numerical simulations based on lava compositions from the anomalous North Atlantics around Iceland indicate that they can be generated by a relatively small increase in mantle temperatures (by 85–210 °C) if subduction of oceanic crustal material was present in the mantle source (Brown & Lesher, 2014). Yet other studies suggest a 125 °C mantle temperature anomaly at ~55–60 Ma, with a significant cooling by 45 Ma (Holbrook et al., 2001), which does not contradict our results for the present-day mantle thermal structure.

A temperature anomaly of 50-100 °C will produce a 0.5–1% change in mantle V_S (Deschamps et al., 2002). This situation explains the on-going debate on the presence of a mantle plume beneath Iceland (Allen, Nolet, et al., 2002; Bijwaard & Spakman, 1999; Delorey et al., 2007; Foulger et al., 2001; Ritsema & Allen, 2003; Shen et al., 2002; Vinnik et al., 2005). The presence of a broad but weak temperature anomaly is consistent with a recent high-resolution global tomography model that images a broadly distributed low-density anomaly in the mantle beneath the Iceland-Jan Mayen region (French & Romanowicz, 2015).

The depth distribution of the temperature anomaly beneath Iceland is, however, not resolved, and the anomaly will be much stronger if it is confined not to the entire upper mantle as assumed in Figure 16c, but to a thin layer. It is, however, difficult to imagine a physical mechanism for a shallow broad mantle temperature anomaly at Iceland, which is also associated with a strong geochemical anomaly (Courtillot et al., 2003). In case the Iceland thermal anomaly is shallow (~100-km deep), it has a better chances to be detected seismically (Figure 17). The expected temperature anomaly at the Azores, as compared to the "normal" ocean, is significantly higher, 100–150 °C if it extends down to the mantle transition zone (Figure 17) and it is consistent with temperature estimates at MORs (Figure 16c; Dalton et al., 2014).

Therefore, our results imply that while a deep temperature anomaly beneath the Azores hot spot can undoubtedly be resolved seismically, it can hardly be resolved beneath Iceland. This situation explains the ambiguity in seismic imaging of a possible mantle plume beneath Iceland.

7. Conclusions

We present 3-D gravity modeling for Europe and the North Atlantics Ocean. The model is constrained by a global compilation for the thickness of sediments (Divins, 2008), the regional updated seismic model for the crust EUNAseis (Artemieva & Thybo, 2013), a global continental model for the lithosphere thickness TC1 (Artemieva et al., 2006), and the half-space cooling model for thickness of the oceanic lithosphere. We calculate mantle residual gravity anomalies and average density of the lithosphere mantle at in situ and SPT (at room P-T) conditions, and conclude the following.

1. The cratonic lithosphere is low dense, with typical SPT densities of 3.32–3.34 g/cm^3. Nondiamondiferous kimberlites are associated with a higher-density subcontinental lithospheric mantle (SCLM).

2. We do not observe any correlation between the age and SCLM density in the East European Craton, which we interpret as evidence for a strong metasomatic reworking of most of the cratonic mantle.
3. High topography of the Norwegian mountains, and especially of the northern dome, may have a strong compositional component as indicated by a low-density SCLM.
4. The absence of a significant difference in mantle SPT density between the cratonic and the Phanerozoic Europe provides support for the isopycnicity hypothesis (Jordan, 1978, 1981) which is roughly satisfied in Europe on the continent scale.
5. The high-density anomaly along the Trans-European Suture Zone (TESZ) from the Black Sea to the North Sea imaged in our model may represent a shallow part of subducting oceanic slab associated with the closure of the Tornquist Ocean. The slab may not be resolved in seismic tomography due to the counter play of composition, low temperature, and high water content.
6. Superdeep basins of Europe and the East Barents Sea are underlain by an extremely dense lithospheric mantle (>3.40 g/cm^3), which requires the presence of 10–20% of eclogitic material. Correlation between the basin depth and the LM density anomaly provides the geophysical evidence that eclogitization is indeed an important mechanism in formation of, at least some, superdeep intraplate basins.
7. Low-density SCLM (3.32–3.34 g/cm^3) beneath the Variscan massifs suggests that small blocks of the cratonic LM of the Gondwana and Laurasia continents could have survived during the Variscan orogeny and are now entrapped within the Phanerozoic lithosphere of Western and Central Europe.
8. Low-density SCLM beneath the French Massif Central and the Rhine Graben may be associated with the presence of a partially molten, low-density material at shallow depths.
9. Mantle density structure of the North Atlantic Ocean is strongly heterogeneous. South of the Charlie Gibbs Fracture Zone (CGFZ), the density structure is well described by the half-space cooling model with significant deviations restricted solely to the hot spots. The largest temperature anomaly is associated with the Azores.
10. A weak low-density anomaly at ~45°N across the North Atlantic Ocean from the Spanish to the Canadian coast may represent a possible, yet unknown, hot spot track with the upper mantle temperature anomaly of ~30–40 °C, if it extends down to a 400-km depth.
11. North of the CGFZ, the entire North Atlantics is anomalous. Strong correlation between the calculated oceanic lithospheric mantle density and geochemical data indicates the presence of a strong chemical heterogeneity in the oceanic mantle, such as caused by melting of subducted oceanic crust, heterogeneity in mantle melting temperatures, and by the presence of continental lithosphere fragments entrapped in oceanic mantle.
12. High density mantle anomaly off-shore East Greenland is compositional in origin, and may be caused by partial eclogitization of basaltic magmas associated with the North Atlantic LIP. The apparent absence of the anomaly at Iceland and along the Greenland-Iceland-Faroe Ridge is caused by the counter-play of a negative low-density anomaly of thermal origin and a positive high-density anomaly of compositional origin.
13. North of the CGFZ, most of the North Atlantics mantle, including the Labrador Sea and the Baffin Bay, has high temperatures and does not follow the half-space cooling model. The anomaly around Iceland can be explained by mantle temperature elevated by less than 50 °C, if it extends down to a 400-km depth. The associated seismic velocity anomaly is at the limit of resolution by tomography models, which explains the on-going debate on the presence of a mantle plume beneath Iceland. In contrast, a significantly stronger mantle temperature anomaly beneath the Azores can be resolved seismically.

Acknowledgments
We appreciate constructive comments and suggestions from two anonymous reviewers. A. S. acknowledges funding by the Research Council of Norway through its Centers of Excellence funding scheme, Project 223272, and Inge Lehmann's grant of the Royal Danish Academy of Sciences and Letters. Research Grant DFF-1323-00053 (the Danish Fund for Independent Research) to I. A. is gratefully acknowledged. The study is based on the published data, which are available as referenced in the article. The updated part of the EUNAseis model is available as supporting information.

References

Afonso, J. C., Ranalli, G., & Fernàndez, M. (2007). Density structure and buoyancy of the oceanic lithosphere revisited. *Geophysical Research Letters*, *34*, L10302. https://doi.org/10.1029/2007GL029515

Afonso, J. C., & Schutt, D. L. (2012). The effects of polybaric partial melting on density and seismic velocities of mantle restites. *Lithos*, *134-135*, 289–303. https://doi.org/10.1016/j.lithos.2012.01.009

Agashev, A. M., Ionov, D. A., Pokhilenko, N. P., Golovin, A. V., Cherepanova, Y., & Sharygin, I. S. (2013). Metasomatism in lithospheric mantle roots: Constraints from whole-rock and mineral chemical composition of deformed peridotite xenoliths from kimberlite pipe Udachnaya. *Lithos*, *160*, 201–215.

Allen, M., Jones, S., Ismail-Zadeh, A., Simmons, M., & Anderson, L. (2002). Onset of subduction as the cause of rapid Pliocene–Quaternary subsidence in the South Caspian Basin. *Geology*, *30*(9), 775–778. https://doi.org/10.1130/0091-7613(2002)030<0775:OOSATC>2.0.CO;2

Allen, R. M., Nolet, G., Morgan, W. J., Vogfjörd, K., Bergsson, B. H., Erlendsson, P., et al. (2002). Imaging the mantle beneath Iceland using integrated seismological techniques. *Journal of Geophysical Research*, *107*(B12), 2325. https://doi.org/10.1029/2001JB000595

Andersen, T., & Sundvoll, B. (1995). Neodymium isotope systematics of the mantle beneath the Baltic shield: Evidence for depleted mantle evolution since the Archaean. *Lithos*, *35*(3-4), 235–243. https://doi.org/10.1016/0024-4937(94)00053-5

Aoki, I., & Takahashi, E. (2004). Density of MORB eclogite in the upper mantle. *Physics of the Earth and Planetary Interiors*, *143-144*, 129–143. https://doi.org/10.1016/j.pepi.2003.10.007

Artemieva, I. M. (2003). Lithospheric structure, composition, and thermal regime of the East European craton: Implications for the subsidence of the Russian Platform. *Earth and Planetary Science Letters*, *213*, 429–444.

Artemieva, I. M. (2006). Global 1°×1° thermal model TC1 for the continental lithosphere: Implications for lithosphere secular evolution. *Tectonophysics*, *416*(1-4), 245–277. https://doi.org/10.1016/j.tecto.2005.11.022

Artemieva, I. M. (2007). Dynamic topography of the East European Craton: shedding light upon the lithospheric structure, composition and mantle dynamics. *Global and Planetary Change*, *58*, 411–434.

Artemieva, I. M. (2009). The continental lithosphere: Reconciling thermal, seismic, and petrologic data. *Lithos*, *109*(1-2), 23–46. https://doi.org/10.1016/j.lithos.2008.09.015

Artemieva, I. M. (2019). The lithosphere structure of the European continent from thermal isostasy. *Earth-Science Reviews*, *188*, 454–468. https://doi.org/10.1016/j.earscirev.2018.11.004

Artemieva, I. M., & Mooney, W. D. (2001). Thermal structure and evolution of Precambrian lithosphere: A global study. *Journal of Geophysical Research*, *106*(B8), 16,387–1,6414. https://doi.org/10.1029/2000JB900439

Artemieva, I. M., & Shulgin, A. (2019). Making and altering the crust: A global perspective on crustal structure and evolution. *Earth and Planetary Science Letters*, *512*, 8–16. https://doi.org/10.1016/j.epsl.2019.01.033

Artemieva, I. M., & Thybo, H. (2013). EUNAseis: A seismic model for Moho and crustal structure in Europe, Greenland, and the North Atlantic region. *Tectonophysics*, *609*, 97–153. https://doi.org/10.1016/j.tecto.2013.08.004

Artemieva, I. M., Thybo, H., & Cherepanova, Y. (2019). Isopycnicity of cratonic mantle restricted to kimberlite provinces. *Earth and Planetary Science Letters*, *505*, 13–19.

Artemieva, I. M., Thybo, H., & Kaban, M. K. (2006). Deep Europe today: Geophysical synthesis of the upper mantle structure and lithospheric processes over 3.5 Ga. *Geological Society, London, Memoirs*, *32*(1), 11–41. https://doi.org/10.1144/GSL.MEM.2006.032.01.02

Artemieva, I. M., & Vinnik, L. P. (2016). Density structure of the cratonic mantle in southern Africa: 2. Correlations with kimberlite distribution, seismic velocities and Moho sharpness. *Gondwana Research*, *36*, 14–27. https://doi.org/10.1016/j.gr.2016.05.002

Artemjev, M. E., Kaban, M. K., Kucherinenko, V. A., Demyanov, G. V., & Taranov, V. A. (1994). Subcrustal density inhomogeneities of Northern Eurasia as derived from the gravity data and isostatic models of the lithosphere. *Tectonophysics*, *240*(1-4), 249–280. https://doi.org/10.1016/0040-1951(94)90275-5

Artyushkov, E. V. (2007). Formation of the superdeep South Caspian basin: Subsidence driven by phase change in continental crust. *Russian Geology and Geophysics*, *48*(12), 1002–1014. https://doi.org/10.1016/j.rgg.2007.11.007

Artyushkov, E. V. (2010). Mechanism of formation of superdeep sedimentary basins: Lithospheric stretching or eclogitization? *Russian Geology and Geophysics*, *51*(12), 1304–1313. https://doi.org/10.1016/j.rgg.2010.11.002

Aulbach, S., Griffin, W. L., Pearson, N. J., & O'Reilly, S. Y. (2013). Nature and timing of metasomatism in the stratified mantle lithosphere beneath the central Slave craton (Canada). *Chemical Geology*, *352*, 153–169. https://doi.org/10.1016/j.chemgeo.2013.05.037

Aulbach, S., & Viljoen, K. S. (2015). Eclogite xenoliths from the Lace kimberlite, Kaapvaal craton: From convecting mantle source to palaeo-ocean floor and back. *Earth and Planetary Science Letters*, *431*, 274–286.

Austrheim, H., Erambert, M., & Engvik, A. K. (1997). Processing of crust in the root of the Caledonian continental collision zone: The role of eclogitization. *Tectonophysics*, *273*, 129–153.

Avchan, G. M., & Oserskaya, M. L. (1985). The petrophysical characteristics of the sedimentary cover of the USSR oil and gas provinces. Nedra, Moscow (192 pp. (in Russian)

BABEL Working Group (1990). Evidence for early Proterozoic plate tectonics from seismic reflection profiles in the Baltic Shield. *Nature*, *348*(6296), 34–38. https://doi.org/10.1038/348034a0

Barrere, C., Ebbing, J., & Gernigon, L. (2011). 3-D density and magnetic crustal characterization of the southwestern Barents Shelf: Implications for the offshore prolongation of the Norwegian Caledonides. *Geophysical Journal International*, *184*(3), 1147–1166. https://doi.org/10.1111/j.1365-246X.2010.04888.x

Barth, M. G., Rudnick, R. L., Horn, I., McDonough, W. F., Spicuzza, M. J., Valley, J. W., & Haggerty, S. E. (2002). Geochemistry of xenolithic eclogites from West Africa, part 2: Origins of the high MgO eclogites. *Geochimica et Cosmochimica Acta*, *66*(24), 4325–4345. https://doi.org/10.1016/S0016-7037(02)01004-9

Barton, P. J. (1986). The relationship between seismic velocity and density in the continental crust – A useful constraint? *Geophysical Journal of the Royal Astronomical Society*, *87*, 195–208. https://doi.org/10.1111/j.1365-246X.1986.tb04553.x

Bercovici, D., Ricard, Y., & Richards, M. A. (2000). The relation between mantle dynamics and plate tectonics: A primer. In M. A. Richards, et al. (Eds.), *The History and Dynamics of Global Plate Motions*, *Geophysical Monography Series*, (Vol. 121, pp. 5–46). Washington, DC: American Geophysical Union.

Beyer, E. E., Griffin, W. L., & O'Reilly, S. Y. (2006). Transformation of Archaean lithospheric mantle by refertilization; evidence from exposed peridotites in theWestern Gneiss region, Norway. *Journal of Petrology*, *47*, 1611–1636.

Bijwaard, H., & Spakman, W. (1999). Tomographic evidence for a narrow whole mantle plume below Iceland. *Earth and Planetary Science Letters*, *166*, 121–126.

Bogdanova, S. V., Bingen, B., Gorbatschev, R., Kheraskova, T. N., Kozlov, V. I., Puchkov, V. N., & Volozh, Y. A. (2008). The East European craton (Baltica) before and during the assembly of Rodinia. *Precambrian Research*, *160*(1-2), 23–45. https://doi.org/10.1016/j.precamres.2007.04.024

Brocher, T. (2005). Empirical relations between elastic wave speeds and density in the Earth's crust. *Bulletin of the Seismological Society of America*, *95*, 2081–2092.

Brown, E. L., & Lesher, C. E. (2014). North Atlantic magmatism controlled by temperature, mantle composition and buoyancy. *Nature Geoscience*, *7*(11), 820–824. https://doi.org/10.1038/ngeo2264

Cadio, C., & Korenaga, J. (2014). Resolving the fine-scale density structure of shallow oceanic mantle by Bayesian inversion of localized geoid anomalies. *Journal of Geophysical Research: Solid Earth*, *119*, 3627–3645. https://doi.org/10.1002/2013JB010840

Carlson, R. L., & Herrick, C. N. (1990). Densities and porosities in the oceanic-crust and their variations with depth and age. *Journal of Geophysical Research*, *95*(B6), 9153–9170. https://doi.org/10.1029/JB095iB06p09153

Carlson, R. W., Pearson, G., & James, D. E. (2005). Physical, chemical, and chronological characteristics of continental mantle. *Reviews of Geophysics*, *43*, RG1001. https://doi.org/10.1029/2004RG000156

Cazenave, A. (1994). The geoid and oceanic lithosphere. In P. Vanicek, & N. T. Christou (Eds.), *Geoid and Geophysical Interpretations*, (pp. 255–284). Boca Raton, FL: CRC Press.

Cherepanova, Y., & Artemieva, I. M. (2015). Density heterogeneity of the cratonic lithosphere: A case study of the Siberian craton. *Gondwana Research*, *28*(4), 1344–1360. https://doi.org/10.1016/j.gr.2014.10.002

Cherepanova, Y., Artemieva, I. M., Thybo, H., & Chemia, Z. (2013). Crustal structure of the Siberian Craton and the West Siberian Basin: An appraisal of existing seismic data. *Tectonophysics*, *609*, 154–183. https://doi.org/10.1016/j.tecto.2013.05.004

Christensen, N. I., & Mooney, W. D. (1995). Seismic velocity structure and composition of the continental crust: A global view. *Journal of Geophysical Research*, *100*(B6), 9761–9788. https://doi.org/10.1029/95JB00259

Cloetingh, S., Ziegler, P. A., Bogaard, P. J. F., Andriessen, P. A. M., Artemieva, I. M., Bada, G., et al., & Topo-Europe working group (2007). Topo-Europe – the geoscience of coupled deep Earth—Surface processes. *Global and Planetary Change*, *58*(1-4), 1–118. https://doi.org/10.1016/j.gloplacha.2007.02.008

Courtillot, V., Davaille, A., Besse, J., & Stock, J. (2003). Three distinct types of hotspots in the Earth's mantle. *Earth and Planetary Science Letters*, *205*(3-4), 295–308. https://doi.org/10.1016/S0012-821X(02)01048-8

Cowie, L., & Kusznir, N. (2018). Renormalisation of global mantle dynamic topography predictions using residual topography measurements for "normal" oceanic crust. *Earth and Planetary Science Letters*, *499*, 145–156. https://doi.org/10.1016/j.epsl.2018.07.018

Dahl-Jensen, T., Larsen, T. B., Woelbern, I., Bach, T., Hanka, W., Kind, R., et al. (2003). Depth to Moho in Greenland: Receiver-function analysis suggests two Proterozoic blocks in Greenland. *Earth and Planetary Science Letters*, *205*(3-4), 379–393. https://doi.org/10.1016/S0012-821X(02)01080-4

Dalton, C. A., Langmuir, C. H., & Gale, A. (2014). Geophysical and Geochemical Evidence for Deep Temperature Variations Beneath Mid-Ocean Ridges. *Science*, *344*(6179), 80–83. https://doi.org/10.1126/science.1249466

Delorey, A. A., Dunn, R. A., & Gaherty, J. B. (2007). Surface wave tomography of the upper mantle beneath the Reykjanes Ridge with implications for ridge–hot spot interaction. *Journal of Geophysical Research*, *112*, B08313. https://doi.org/10.1029/2006JB004785

Deschamps, F., Snieder, R., & Trampert, J. (2001). The relative density-to-shear velocity scaling in the uppermost mantle. *Physics of the Earth and Planetary Interiors*, *124*(3-4), 193–212. https://doi.org/10.1016/S0031-9201(01)00199-6

Deschamps, F., Trampert, J., & Snieder, R. (2002). Anomalies of temperature and iron in the uppermost mantle inferred from gravity data and tomographic models. *Physics of the Earth and Planetary Interiors*, *129*(3-4), 245–264. https://doi.org/10.1016/S0031-9201(01)00294-1

Divins, D. L. (2008). NGDC total sediment thickness of the world's oceans and marginal seas. http://www.ngdc.noaa.gov/mgg/sedthick/sedthick.html

Doin, M.-P., Fleitout, L., & Christensen, U. R. (1997). Mantle convection and stability of depleted and undepleted continental lithosphere. *Journal of Geophysical Research*, *102*(B2), 2771–2787. https://doi.org/10.1029/96JB03271

Dore, A. G. (1995). Barents Sea geology, petroleum resources and commercial potential. *Arctic*, *48*(3), 207–221.

Doring, J., Götze, H. J., & Kaban, M. K. (1997). Preliminary study of the gravity field of the southern Urals along the URSEIS 95 seismic profile. *Tectonophysics*, *276*(1-4), 49–62. https://doi.org/10.1016/S0040-1951(97)00047-4

Doucet, L. S., Peslier, A. H., Ionov, D. A., Brandon, A. D., Golovin, A. V., Goncharov, A. G., & Ashchepkov, I. V. (2014). High water contents in the Siberian cratonic mantle linked to metasomatism: An FTIR study of Udachnaya peridotite xenoliths. *Geochimica et Cosmochimica Acta*, *137*, 159–187. https://doi.org/10.1016/j.gca.2014.04.011

Downes, H., Reichow, M. K., Mason, P. R., Beard, A. D., & Thirlwall, M. (2003). Mantle domains in the lithosphere beneath the French Massif Central: Trace element and isotopic evidence from mantle clinopyroxenes. *Chemical Geology*, *200*, 71–87.

Drachev, S. S., Malyshev, N. A., & Nikishin, A. M. (2010). Tectonic history and petroleum geology of the Russian Arctic Shelves: An overview. *Petroleum Geology Conference Series*, *7*, 591–619.

Dufrechou, G., Tiberi, C., Martin, R., Bonvalot, S., Chevrot, S., & Seoane, L. (2018). Deep structure of Pyrenees range (SW Europe) imaged by joint inversion of gravity and teleseismic delay time. *Geophysical Journal International*, *214*(1), 282–301. https://doi.org/10.1093/gji/ggy134

Eaton, D. W., & Perry, H. K. C. (2013). Ephemeral isopycnicity of cratonic mantle keels. *Nature Geoscience*, *6*, 967–970.

Eken, T., Plomerová, J., Vecsey, L., Babuška, V., Roberts, R., Shomali, H., & Bodvarsson, R. (2012). Effects of seismic anisotropy on *P*-velocity tomography of the Baltic Shield. *Geophysical Journal International*, *188*(2), 600–612. https://doi.org/10.1111/j.1365-246X.2011.05280.x

EXXON (1985). Tectonic map of the world. Scale 1:10,000,000. Exxon Prod. Research Co., AAPGF, Tulsa, OK, USA.

Faul, U. H., & Jackson, I. (2005). The seismological signature of temperature and grain size variations in the upper mantle. *Earth and Planetary Science Letters*, *234*(1-2), 119–134. https://doi.org/10.1016/j.epsl.2005.02.008

Ficini, E., Dal Zilio, L., Doglioni, C., & Gerya, T. V. (2017). Horizontal mantle flow controls subduction dynamics. *Nature Scientific Reports*, *7*, 1–26. https://doi.org/10.1038/s41598-017-06551-y

Forte, A. M., & Perry, A. C. (2000). Seismic-geodynamic evidence for a chemically depleted continental tectosphere. *Science*, *290*(5498), 1940–1944. https://doi.org/10.1126/science.290.5498.1940

Foulger, G. R., Panza, G. F., Artemieva, I. M., Bastow, I. D., Cammarano, F., Evans, J. R., et al. (2013). Caveats on tomographic images. *Terra Nova*, *25*(4), 259–281. https://doi.org/10.1111/ter.12041

Foulger, G. R., Pritchard, M. J., Julian, B. R., Evans, J. R., Allen, R. M., Nolet, G., et al. (2001). Seismic tomography shows that upwelling beneath Iceland is confined to the upper mantle. *Geophysical Journal International*, *146*(2), 504–530. https://doi.org/10.1046/j.0956-540x.2001.01470.x

Franke, W. (1994). Exhumierung von Eklogiten im Saxothuringikum. Orogene Prozesse. *Terra Nostra*, *3*(94), 38.

French, S. W., & Romanowicz, B. (2015). Broad plumes rooted at the base of the Earth's mantle beneath major hotspots. *Nature*, *525*(7567), 95–99. https://doi.org/10.1038/nature14876

Fry, B., Deschamps, F., Kissling, E., Stehly, L., & Giardini, D. (2010). Layered azimuthal anisotropy of Rayleigh wave phase velocities in the European Alpine lithosphere inferred from ambient noise. *Earth and Planetary Science Letters*, *297*(1-2), 95–102. https://doi.org/10.1016/j.epsl.2010.06.008

Gabrielsen, R. H., Faleide, J. I., Pascal, C., Braathen, A., Nystuen, J. P., Etzelmuller, B., & O'Donnell, S. (2010). Latest Caledonian to Present tectono-morphogical development of southern Norway. *Marine and Petroleum Geology*, *27*(3), 709–723. https://doi.org/10.1016/j.marpetgeo.2009.06.004

Gac, S., Huismans, R., Simon, N., Faleide, J. I., & Podladchikov, Y. (2014). Effects of Lithosphere buckling on subsidence and hydrocarbon maturation: A case-study from the ultra-deep East Barents Sea basin. *Earth and Planetary Science Letters*, *407*, 123–133.

Gao, S., Rudnick, R. L., Carlson, R. W., McDonough, W. F., & Liu, Y. S. (2002). Re-Os evidence for replacement of ancient mantle lithosphere beneath the North China craton. *Earth and Planetary Science Letters*, *198*(3-4), 307–322. https://doi.org/10.1016/S0012-821X(02)00489-2

Gaul, O. F., Griffin, W. L., O'Reilly, S. Y., & Pearson, N. J. (2000). Mapping olivine composition in the lithospheric mantle. *Earth and Planetary Science Letters*, *182*(3-4), 223–235. https://doi.org/10.1016/S0012-821X(00)00243-0

GEBCO: General Bathymetric Chart of the Oceans (2010). GEBCO_08 grid, version 20100927. (Available at http://www.gebco.net), British Oceanographic Data Center, Liverpool, U.K.

Godey, S., Deschamps, F., Trampert, J., & Snieder, R. (2004). Thermal and compositional anomalies beneath the North American continent. *Journal of Geophysical Research*, *109*, B01308. https://doi.org/10.1029/2002JB002263

Goes, S., Govers, R., & Vacher, P. (2000). Shallow upper mantle temperatures under Europe from P and *S* wave tomography. *Journal of Geophysical Research*, *105*(B5), 11,153–11,169. https://doi.org/10.1029/1999JB900300

Goes, S., Simons, F., & Yoshizawa, K. (2005). Seismic constraints on temperature of the Australian uppermost mantle. *Earth and Planetary Science Letters*, *236*(1-2), 227–237. https://doi.org/10.1016/j.epsl.2005.05.001

Grad, M., Tiira, T., & ESC Moho Working Group (2009). The Moho depth of the European plate. *Geophysical Journal International*, *176*, 279–292.

Griffin, W. L., Natapov, L. M., O'Reilly, S. Y., van Achterbergh, E., Cherenkova, A. F., & Cherenkov, V. G. (2005). The Kharamai kimberlite field, Siberia: Modification of the lithospheric mantle by the Siberian Trap event. *Lithos*, *81*(1-4), 167–187. https://doi.org/10.1016/j.lithos.2004.10.001

Griffin, W. L., O'Reilly, S. Y., Doyle, B. J., Pearson, N. J., Coopersmith, H., Kivi, K., et al. (2004). Lithospheric mapping beneath the North American Plate. *Lithos*, *77*(1-4), 873–922. https://doi.org/10.1016/j.lithos.2004.03.034

Griffin, W. L., O'Reilly, S. Y., Ryan, C. G., Gaul, O., & Ionov, D. (1998). Secular variation in the composition of continental lithospheric mantle. In J. Braun, et al. (Eds.), *Structure and Evolution of the Australian Continent*, *AGU Geodynamics Series*, (Vol. 26, pp. 1–25). Washington, DC: American Geophysical Union. https://doi.org/10.1029/GD026p0001

Haase, C., Ebbing, J., & Funck, T. (2017). A 3D regional crustal model of the NE Atlantic based on seismic and gravity data. *Geological Society, London, Special Publications*, *447*(1), 233–247. https://doi.org/10.1144/SP447.8

Harrison, L. N., Weis, D., & Garcia, M. O. (2017). The link between Hawaiian mantle plume composition, magmatic flux, and deep mantle geodynamics. *Earth and Planetary Science Letters*, *463*, 298–309. https://doi.org/10.1016/j.epsl.2017.01.027

Hawkesworth, C. J., Erlank, A. J., Kempton, P. D., & Waters, F. G. (1990). Mantle metasomatism: Isotope and trace-element trends in xenoliths from Kimberley, South Africa. *Chemical Geology*, *85*(1-2), 19–34. https://doi.org/10.1016/0009-2541(90)90121-M

Hejrani, B., Balling, N., Jacobsen, B. H., & England, R. (2017). Upper-mantle velocities below the Scandinavian Mountains from *P*- and *S*-wave traveltime tomography. *Geophysical Journal International*, *208*(1), 177–192. https://doi.org/10.1093/gji/ggw370

Herceg, M., Artemieva, I. M., & Thybo, H. (2016). Sensitivity analysis of crustal correction for calculation of lithospheric mantle density from gravity data. *Geophysical Journal International*, *204*, 738–747.

Hetenyi, G., Molinari, I., Clinton, J., Bokelmann, G., Bondár, I., Crawford, W. C., et al. (2018). The AlpArray seismic network: A large-scale European experiment to image the Alpine orogen. *Surveys in Geophysics*, *39*(5), 1009–1033. https://doi.org/10.1007/s10712-018-9472-4

Holbrook, W. S., Larsen, H. C., Korenaga, J., Dahl-Jensen, T., Reid, I. D., Kelemen, P. B., et al. (2001). Mantle thermal structure and active upwelling during continental breakup in the North Atlantic. *Earth and Planetary Science Letters*, *190*(3-4), 251–266. https://doi.org/10.1016/S0012-821X(01)00392-2

Howarth, G. H., Barry, P. H., Pernet-Fisher, J. F., Baziotis, I. P., Pokhilenko, N. P., Pokhilenko, L. N., et al. (2014). Superplume metasomatism: Evidence from Siberian mantle xenoliths. *Lithos*, *184*, 209–224.

Huang, J. X., Griffin, W. L., Gréau, Y., Pearson, N. J., O'Reilly, S. Y., Cliff, J., & Martin, L. (2014). Unmasking xenolithic eclogites: Progressive metasomatism of a key Roberts Victor sample. *Chemical Geology*, *364*, 56–65. https://doi.org/10.1016/j.chemgeo.2013.11.025

Irifune, T. (1987). An experimental investigation of the pyroxene-garnet transformation in a pyrolite composition and its bearing on the composition of the mantle. *Physics of the Earth and Planetary Interiors*, *45*, 324–336.

Jacob, D., Jagoutz, E., Lowry, D., Mattey, D., & Kudrjavtseva, G. (1994). Diamondiferous eclogites from Siberia—Remnants of Archean oceanic-crust. *Geochimica et Cosmochimica Acta*, *58*(23), 5191–5207. https://doi.org/10.1016/0016-7037(94)90304-2

James, D., Boyd, F., Schutt, D., Bell, D., & Carlson, R. (2004). Xenolith constraints in seismic velocities in the upper mantle beneath southern Africa. *Geochemistry, Geophysics, Geosystems*, *5*, Q01002. https://doi.org/10.1029/2003GC000551

Jaupart, C., & Mareschal, J.-C. (1999). Thermal structure and thickness of continental roots. *Lithos*, *48*(1-4), 93–114. https://doi.org/10.1016/S0024-4937(99)00023-7

Jordan, T. H. (1975). The continental tectosphere. *Reviews of Geophysics and Space Physics*, *13*(3), 1–12. https://doi.org/10.1029/RG013i003p00001

Jordan, T. H. (1978). Composition and development of the continental tectosphere. *Nature*, *274*, 544–548.

Jordan, T. H. (1979). Mineralogies, densities and seismic velocities of garnet lherzolites and their geophysical implications. In F. R. Boyd, & H. O. A. Meyer (Eds.), *The mantle sample: Inclusions in kimberlite and other volcanics*. Proc. Second Intern. kimberlite Conf., (Vol. 2, pp. 1–14). Washington, DC: American Geophysical Union.

Jordan, T. H. (1981). Continents as a chemical boundary layer. *Philosophical Transactions of the Royal Society of London A*, *301*(1461), 359–373. https://doi.org/10.1098/rsta.1981.0117

Jordan, T. H. (1988). Structure and formation of the continental tectosphere. *Journal of Petrology, Special Lithosphere Issue*, *29*, 11–37.

Kaban, M. K., & Mooney, W. D. (2001). Density structure of the lithosphere in the southwestern United States and its tectonic significance. *Journal of Geophysical Research*, *106B*, 721–740.

Kaban, M. K., & Schwintzer, P. (2001). Oceanic upper mantle structure from experimental scaling of V_s and density at different depths. *Geophysical Journal International*, *147*, 199–214.

Kaban, M. K., Schwintzer, P., Artemieva, I. M., & Mooney, W. D. (2003). Density of the continental roots: Compositional and thermal effects. *Earth and Planetary Science Letters*, *209*, 53–69.

Kaban, M. K., Schwintzer, P., & Tikhotsky, S. A. (1999). Global isostatic gravity model of the Earth. *Geophysical Journal International*, *136*(3), 519–536. https://doi.org/10.1046/j.1365-246x.1999.00731.x

Kaban, M. K., Stolk, W., Tesauro, M., el Khrepy, S., al-Arifi, N., Beekman, F., & Cloetingh, S. A. P. L. (2016). 3D density model of the upper mantle of Asia based on inversion of gravity and seismic tomography data. *Geochemistry, Geophysics, Geosystems*, *17*, 4457–4477. https://doi.org/10.1002/2016GC006458

Karato, S. I., Olugboji, T., & Park, J. (2015). Mechanisms and geologic significance of the mid-lithosphere discontinuity in the continents. *Nature Geoscience*, *8*(7), 509–514. https://doi.org/10.1038/ngeo2462

Kargin, A. V., Sazonova, L. V., Nosova, A. A., & Tretyachenko, V. V. (2016). Composition of garnet and clinopyroxene in peridotite xenoliths from the Grib kimberlite pipe, Arkhangelsk diamond province, Russia: Evidence for mantle metasomatism associated with kimberlite melts. *Lithos*, *262*, 442–455.

Kashubin, S., Petrov, O. V., Artemieva, I. M., Morozov, A. F., Vyatkina, D. V., Golysheva, Y. S., et al. (2018). Crustal structure of the Mendeleev Rise and the Chukchi Plateau (Arctic Ocean) along the Russian wide-angle and multichannel seismic reflection experiment "Arctic-2012". *Journal of Geodynamics*, *119*, 107–122. https://doi.org/10.1016/j.jog.2018.03.006

Kastle, E. D., El-Sharkawy, A., Boschi, L., Meier, T., Rosenberg, C., Bellahsen, N., et al. (2018). Surface wave tomography of the alps using ambient-noise and earthquake phase velocity measurements. *Journal of Geophysical Research: Solid Earth*, *123*, 1770–1792. https://doi.org/10.1002/2017JB014698

Kelemen, P. B., & Behn, M. D. (2016). Formation of lower continental crust by relamination of buoyant arc lavas and plutons. *Nature Geoscience*, *9*(3), 197–205. https://doi.org/10.1038/ngeo2662

Kelly, R. K., Kelemen, P. B., & Jull, M. (2003). Buoyancy of the continental upper mantle. *Geochemistry, Geophysics, Geosystems*, *4*(2), 1017. https://doi.org/10.1029/2002GC000399

Kennett, B. L. N., Salmon, M., Saygin, E., & AusMoho Working Group (2011). AusMoho: The variation of Moho depth in Australia. *Geophysical Journal International*, *187*, 946–958.

Kopylova, M. G., Beausoleil, Y., Goncharov, A., Burgess, J., & Strand, P. (2016). Spatial distribution of eclogite in the Slave cratonic mantle: The role of subduction. *Tectonophysics*, *672*(673), 87–103.

Korenaga, J. (2013). Initiation and evolution of plate tectonics on Earth: Theories and observations. *Annual Review of Earth and Planetary Sciences*, *41*(1), 117–151. https://doi.org/10.1146/annurev-earth-050212-124208

Korenaga, J., & Kelemen, P. B. (2000). Major element heterogeneity in the mantle source of the North Atlantic igneous province. *Earth and Planetary Science Letters*, *184*(1), 251–268. https://doi.org/10.1016/S0012-821X(00)00308-3

Kraft, H. A., Thybo, H., Vinnik, L. P., & Oreshin, S. (2019). Crustal structure in central-eastern Greenland from receiver functions. *Journal of Geophysical Research: Solid Earth*, *124*, 1653–1670. https://doi.org/10.1029/2018JB015919

Kustowski, B., Ekström, G., & Dziewoński, A. M. (2008). The shear-wave velocity structure in the upper mantle beneath Eurasia. *Geophysical Journal International*, *174*(3), 978–992. https://doi.org/10.1111/j.1365-246X.2008.03865.x

Lahtinen, R., Korja, A., & Nironen, M. (2005). Chapter 11: Paleoproterozoic tectonic evolution. *Developments in Precambrian Geology*, *14*, 481–531.

Laske, G., Masters, G., Ma, Z., Pasyanos, M. (2013). Update on CRUST1.0—A 1-degree global model of Earth's crust. *Geophysical Research Abstracts*, 15, Abstract EGU2013, 2658.

Lebedev, S., Schaeffer, A. J., Fullea, J., & Pease, V. (2018). Seismic tomography of the Arctic region: Inferences for the thermal structure and evolution of the lithosphere. *Geological Society, London, Special Publications*, *460*(1), 419–440. https://doi.org/10.1144/SP460.10

Lee, C.-T., Lenardic, A., Cooper, C. M., Niu, F., & Levander, A. (2004). The role of chemical boundary layers in regulating the thickness of continental and oceanic thermal boundary layers. *Earth and Planetary Science Letters*, *230*, 379–395.

Lee, C.-T. A. (2003). Compositional variation of density and seismic velocities in natural peridotites at STP conditions: Implications for seismic imaging of compositional heterogeneities in the upper mantle. *Journal of Geophysical Research*, *108*(B9), 2441. https://doi.org/10.1029/2003JB002413

Legendre, C. P., Meier, T., Lebedev, S., Friederich, W., & Viereck-Götte, L. (2012). A shear wave velocity model of the European upper mantle from automated inversion of seismic shear and surface waveforms. *Geophysical Journal International*, *191*(1), 282–304. https://doi.org/10.1111/j.1365-246X.2012.05613.x

Lehtonen, M., O'Brien, H. E., Peltonen, P., Johanson, B. S., & Pakkanen, L. (2004). Layered mantle at the Karelian Craton margin: P-T of mantle xenocrysts and xenoliths from the Kaavi–Kuopio kimberlites, Finland. *Lithos*, *77*(1-4), 593–608. https://doi.org/10.1016/j.lithos.2004.04.026

Lenardic, A., & Moresi, L. N. (1999). Some thoughts on the stability of cratonic lithosphere: Effects of buoyancy and viscosity. *Journal of Geophysical Research*, *104*(B6), 12,747–12,758. https://doi.org/10.1029/1999JB900035

Levshin, A. L., Schweitzer, J., Weidle, C., Shapiro, N. M., & Ritzwoller, M. H. (2007). Surface wave tomography of the Barents Sea and surrounding regions. *Geophysical Journal International*, *170*(1), 441–459. https://doi.org/10.1111/j.1365-246X.2006.03285.x

Lippitsch, R., Kissling, E., & Ansorge, J. (2003). Upper mantle structure beneath the Alpine orogen from high-resolution teleseismic tomography. *Journal of Geophysical Research*, *108*(B8), 2376. https://doi.org/10.1029/2002JB002016

Lu, Y., Stehly, L., & Paul, A. (2018). High-resolution surface wave tomography of the European crust and uppermost mantle from ambient seismic noise. *Geophysical Journal International*, *214*(2), 1136–1150. https://doi.org/10.1093/gji/ggy188

Ludwig, W. F., Nafe, J. E., & Drake, C. L. (1970). Seismic refraction. In A. E. Maxwell (Ed.), *The sea. Ideas and observations on progress in the study of the seas* (Vol. 4, pp. 53–84). Wiley-Interscience: New York.

Lundin, E. R., & Dore, A. G. (2005). Fixity of the Iceland "hotspot" on the Mid-Atlantic Ridge: Observational evidence, mechanisms, and implications for Atlantic volcanic margins. In G. R. Foulger, J. H. Natland, D. C. Presnall, & D. L. Anderson (Eds.), *Plates, plumes, and paradigms*, *Geological Society of America, Special Paper* (Vol. 388, pp. 627–652). Boulder, CO

Matte, P. (1986). Tectonics and plate tectonics model for the Variscan Belt of Europe. *Tectonophysics*, *126*(2-4), 329–374. https://doi.org/10.1016/0040-1951(86)90237-4

Maupin, V., Agostini, A., Artemieva, I., Balling, N., Beekman, F., Ebbing, J., et al. (2013). The deep structure of the Scandes and possible relations to its tectonic history and present topography. *Tectonophysics*, *602*, 15–37. https://doi.org/10.1016/j.tecto.2013.03.010

Maystrenko, Y., & Scheck-Wenderoth, M. (2009). Density contrasts in the upper mantle and lower crust across the continent–ocean transition: Constraints from 3-D gravity modelling at the Norwegian margin. *Geophysical Journal International*, *179*(1), 536–548.

Menard, G., & Molnar, P. (1988). Collapse of a Hercynian Tibetan plateau into a late Paleozoic European basin and range province. *Nature*, *334*(6179), 235–237. https://doi.org/10.1038/334235a0

Molnar, P., England, P. C., & Jones, C. H. (2015). Mantle dynamics, isostasy, and the support of high terrain. *Journal Geophysical Research: Solid Earth*, *120*, 1932–1957. https://doi.org/10.1002/2014JB011724

Mooney, W. D., & Kaban, M. K. (2010). The North American upper mantle: Density, composition, and evolution. *Journal of Geophysical Research*, *115*, B12424. https://doi.org/10.1029/2010JB000866

Mooney, W. D., & Vidale, J. (2003). Thermal and chemical variations in subcrustal cratonic lithosphere: Evidence from crustal isostasy. *Lithos*, *71*, 185–193.

Mosar, J., Torsvik, T., & Bat Team (2002). Opening the Norwegian and Greenland Seas: Plate tectonics in mid Norway since the Late Permian. In E. A. Eide (Ed.), *BATLAS - Mid Norway plate reconstruction Atlas with global and Atlantic perspectives*, (pp. 18–39). Norway: Geological Survey of Norway.

Nielsen, S. B., Gallagher, K., Leighton, C., Balling, N., Svenningsen, L., Jacobsen, B. H., et al. (2012). The evolution of western Scandinavian topography: A review of Neogene uplift versus the ICE (isostasy–climate–erosion) hypothesis. *Journal of Geodynamics*, *47*(2–3), 72–95.
Nolet, G., & Zuilhuis, A. (1994). Low S-velocities under the Tornquist-Teisseyre zone—Evidence for water injection into the transition zone by subduction. *Geophysical Journal International*, *99*(B8), 15,813–15,820. https://doi.org/10.1029/94JB00083
O'Hara, M. J. (1975). Is there an Icelandic mantle plume? *Nature*, *253*(5494), 708–710. https://doi.org/10.1038/253708a0
O'Neill, C., Lenardic, A., Moresi, L., Torsvik, T. H., & Lee, C.-T. (2007). Episodic Precambrian subduction. *Earth and Planetary Science Letters*, *262*(3-4), 552–562. https://doi.org/10.1016/j.epsl.2007.04.056
Oserskaya, M. L., & Podoba, N. V. (Eds.) (1967). Physical properties of sediment cover of USSR territory. *Nedra*, Moscow (772 pp. (in Russian).
Panasyuk, S. V., & Hager, B. H. (2000). Models of isostatic and dynamic topography, geoid anomalies, and their uncertainties. *Journal of Geophysical Research*, *105B*, 28,199–28,209. https://doi.org/10.1029/2000JB900249
Parkin, C. J., & White, R. S. (2008). Influence of the Iceland mantle plume on oceanic crust generation in the North Atlantic. *Geophysical Journal International*, *173*(1), 168–188. https://doi.org/10.1111/j.1365-246X.2007.03689.x
Pavlis, N. K., Holmes, S. A., Kenyon, S. C., & Factor, J. K. (2012). The development and evaluation of the Earth Gravitational Model 2008 (EGM2008). *Journal of Geophysical Research*, *117*, B04406. https://doi.org/10.1029/2011JB008916
Pedersen, H. A., Debayle, E., Maupin, V., & the POLENET/LAPNET Working Group (2013). Strong lateral variations of lithospheric mantle beneath cratons—Example from the Baltic Shield. *Earth and Planetary Science Letters*, *383*, 164–172.
Peslier, A. H., Woodland, A. B., Bell, D. R., & Lazarov, M. (2010). Olivine water contents in the continental lithosphere and the longevity of cratons. *Nature*, *467*(7311), 78–81. https://doi.org/10.1038/nature09317
Pilidou, S., Priestley, K., Gudmundsson, O., & Debayle, E. (2004). Upper mantle S-wave speed heterogeneity and anisotropy beneath the North Atlantic from regional surface wave tomography: The Iceland and Azores plumes. *Geophysical Journal International*, *159*(3), 1057–1076. https://doi.org/10.1111/j.1365-246X.2004.02462.x
Plomerová, J., Babušhka, V., Sileny, J., & Horalek, J. (1998). Seismic anisotropy and velocity variations in the mantle beneath the Saxothuringicum–Moldanubicum contact in central Europe. *Pure and Applied Geophysics*, *151*(4), 365–394. https://doi.org/10.1007/s000240050118
Plomerová, J., & Babuška, V. (2010). Long memory of mantle lithosphere fabric—European LAB constrained from seismic anisotropy. *Lithos*, *120*(1-2), 131–143. https://doi.org/10.1016/j.lithos.2010.01.008
Poudjom Djomani, Y. H., O'Reilly, S. Y., Griffin, W. L., & Morgan, P. (2001). The density structure of subcontinental lithosphere through time. *Earth and Planetary Science Letters*, *184*, 605–621.
Ricard, Y., Richard, M., Lithgow-Bertelloni, C., & Le Stunff, Y. (1993). A geodynamic model of mantle density heterogeneity. *Journal of Geophysical Research*, *98B*, 21,895–21,909. https://doi.org/10.1029/93JB02216
Ritsema, J., & Allen, R. M. (2003). The elusive mantle plume. *Earth and Planetary Science Letters*, *207*, 1–12.
Ritzwoller, M. H., & Levshin, A. L. (1998). Eurasian surface wave tomography: Group velocities. *Journal of Geophysical Research*, *103*(B3), 4839–4878. https://doi.org/10.1029/97JB02622
Ryberg, T., Wenzel, F., Mechie, J., Egorkin, A., Fuchs, K., & Solodilov, L. (1996). Two-dimensional velocity structure beneath Northern Eurasia derived from the super long-range seismic profile Quartz. *Bulletin of the Seismological Society of America*, *86*, 857–867.
Schaefer, B. F., Turner, S., Parkinson, I., Rogers, N., & Hawkesworth, C. (2002). Evidence for recycled Archaean oceanic mantle lithosphere in the Azores plume. *Nature*, *420*(6913), 304–307.
Schaeffer, A. J., & Lebedev, S. (2013). Global shear speed structure of the upper mantle and transition zone. *Geophysical Journal International*, *194*(1), 417–449. https://doi.org/10.1093/gji/ggt095
Schiffer, C., Balling, N., Jacobsen, B. H., Stephenson, R. A., & Nielsen, S. B. (2014). Seismological evidence for a fossil subduction zone in the East Greenland Caledonides. *Geology*, *42*(4), 311–314. https://doi.org/10.1130/G35244.1
Schivardi, R., & Morelli, A. (2009). Surface wave tomography in the European and Mediterranean region. *Geophysical Journal International*, *177*, 1050–1066.
Schubert, G., Turcotte, D. L., & Olson, P. (2001). *Mantle Convection in the Earth and Planets*. Cambridge, U.K: Cambridge Univ. Press. https://doi.org/10.1017/CBO9780511612879
Schulze, D. J. (1989). Constraints on the abundance of eclogite in the upper mantle. *Journal of Geophysical Research*, *94*(B4), 4205–4212. https://doi.org/10.1029/JB094iB04p04205
Schulze, D. J., Valley, J. W., & Spicuzza, M. J. (2000). Coesite eclogites from the Roberts Victor kimberlite, South Africa. *Lithos*, *54*, 23–32.
Schutt, D. L., & Lesher, C. E. (2006). Effects of melt depletion on the density and seismic velocity of garnet and spinel lherzolite. *Journal of Geophysical Research*, *111*, B05401. https://doi.org/10.1029/2003JB002950
Shapiro, S. S., Hager, B. H., & Jordan, T. H. (1999). Stability and dynamics of the continental tectosphere. *Lithos*, *48*, 135–152.
Shen, Y., Solomon, S. C., Bjarnason, I. T., Nolet, G., Morgan, W. J., Allen, R. M., et al. (2002). Seismic evidence for a tiled mantle plume and north–south mantle flow beneath Iceland. *Earth and Planetary Science Letters*, *197*(3-4), 261–272. https://doi.org/10.1016/S0012-821X(02)00494-6
Shirey, S. B., Carlson, R. W., Richardson, S. H., Menzies, A., Gurney, J. J., Pearson, D. G., et al. (2001). Archean emplacement of eclogitic components into the lithospheric mantle during formation of the Kaapvaal Craton. *Geophysical Research Letters*, *28*(13), 2509–2512. https://doi.org/10.1029/2000GL012589
Shulgin, A., & Thybo, H. (2014). Crustal structure of the Central-Eastern Greenland: Results from the Topo Greenland refraction profile. Geophysical Research Abstracts, vol. 16, 9008.
Silvennoinen, H., Kozlovskaya, E., & Kissling, E. (2016). POLENET/LAPNET teleseismic *P*-wave travel time tomography model of the upper mantle beneath northern Fennoscandia. *Solid Earth*, *7*, 425–439.
Simmons, N. A., Forte, A. M., & Grand, S. P. (2009). Joint seismic, geodynamic and mineral physical constraints on three-dimensional mantle heterogeneity: Implications for the relative importance of thermal versus compositional heterogeneity. *Geophysical Journal International*, *177*(3), 1284–1304. https://doi.org/10.1111/j.1365-246X.2009.04133.x
Simon, N., Neumann, E. R., Bonadiman, C., Coltorti, M., Delpech, G., Grégoire, M., & Widom, E. (2008). Ultra-refractory domains in the oceanic mantle lithosphere sampled as mantle xenoliths at ocean islands. *Journal of Petrology*, *49*(6), 1223–1251. https://doi.org/10.1093/petrology/egn023
Simon, N., & Podladchikov, Y. Y. (2008). The effect of mantle composition on density in the extending lithosphere. *Earth and Planetary Science Letters*, *272*(1-2), 148–157. https://doi.org/10.1016/j.epsl.2008.04.027
Sizova, E., Gerya, T., Brown, M., & Perchuk, L. L. (2010). Subduction styles in the Precambrian: Insight from numerical experiments. *Lithos*, *116*(3-4), 209–229. https://doi.org/10.1016/j.lithos.2009.05.028

Sleep, N. H. (2005). Evolution of the continental lithosphere. *Annual Review of Earth and Planetary Sciences*, *33*(1), 369–393. https://doi.org/10.1146/annurev.earth.33.092203.122643

Smart, K. A., Chacko, T., Stachel, T., Tappe, S., Stern, R. A., & Ickert, R. B. (2012). Eclogite formation beneath the northern Slave craton constrained by diamond inclusions: Oceanic lithosphere origin without a crustal signature. *Earth and Planetary Science Letters*, *319*, 165–177.

Steinberger, B. (2016). Topography caused by mantle density variations: Observation-based estimates and models derived from tomography and lithosphere thickness. *Geophysical Journal International*, *205*(1), 604–621.

Szwillus, W., Ebbing, J., & Holzrichter, N. (2016). Importance of far-field topographic and isostatic corrections for regional density modeling. *Geophysical Journal International*, *207*(1), 274–287. https://doi.org/10.1093/gji/ggw270

Tan, P., Sippel, J., Breivik, A. J., Meesen, C., & Scheck-Wenderoth, M. (2018). Lithospheric control on asthenospheric flow from the Iceland plume: 3-D density modeling of the Jan Mayen-East Greenland Region, NE Atlantic. *Journal of Geophysical Research: Solid Earth*, *123*, 9223–9248. https://doi.org/10.1029/2018JB015634

Tesauro, M., Kaban, M., Mooney, W. D., & Cloetingh, S. (2014). NACr14: A 3D model for the crustal structure of the North American Continent. *Tectonophysics*, *631*. https://doi.org/10.1016/j.tecto.2014.04.016

Tondi, R., Schivardi, R., Molinari, I., & Morelli, A. (2012). Upper mantle structure below the European continent: Constraints from surface-wave tomography and GRACE satellite gravity data. *Journal of Geophysical Research*, *117*, B09401. https://doi.org/10.1029/2012JB009149

Uenver-Thiele, L., Woodland, A. B., Seitz, H. M., Downes, H., & Altherr, R. (2017). Metasomatic processes revealed by trace element and redox signatures of the lithospheric mantle beneath the Massif Central, France. *Journal of Petrology*, *58*(3), 395–422. https://doi.org/10.1093/petrology/egx020

Uieda, L., Barbosa, V., & Braitenberg, C. (2016). Tesseroids: Forward-modeling gravitational fields in spherical coordinates. *Geophysics*, *81*(5), F41–F48. https://doi.org/10.1190/geo2015-0204.1

Vigneresse, J. L. (2005). The specific case of the Mid-Proterozoic rapakivi granites and associated suite within the context of the Columbia supercontinent. *Precambrian Research*, *137*(1-2), 1–134. https://doi.org/10.1016/j.precamres.2005.01.001

Villasenor, A., Ritzwoller, M. H., Levshin, A. L., Barmin, M. P., Engdahl, E. R., Spakman, W., & Trampert, J. (2001). Shear velocity structure of central Eurasia from inversion of surface wave velocities. *Physics of the Earth and Planetary Interiors*, *123*(2-4), 169–184. https://doi.org/10.1016/S0031-9201(00)00208-9

Vinnik, L. P., Foulger, G. R., & Du, Z. (2005). Seismic boundaries in the mantle beneath Iceland: A new constraint on temperature. *Geophysical Journal International*, *160*(2), 533–538. https://doi.org/10.1111/j.1365-246X.2005.02529.x

Weidle, C., & Maupin, V. (2008). An upper-mantle S-wave velocity model for Northern Europe from Love and Rayleigh group velocities. *Geophysical Journal International*, *175*(3), 1154–1168. https://doi.org/10.1111/j.1365-246X.2008.03957.x

Werling, F., & Altherr, R. (1997). Thermal evolution of the lithosphere beneath the French Massif Central as deduced from geothermobarometry on mantle xenoliths. *Tectonophysics*, *275*(1-3), 119–141. https://doi.org/10.1016/S0040-1951(97)00018-8

Widom, E. (2002). Ancient mantle in a modern plume. *Nature*, *420*, 281–282.

Wittig, N., Baker, J. A., & Downes, H. (2006). Dating the mantle roots of the young continental crust. *Geology*, *34*, 237–240.

Xia, B., Thybo, H., & Artemieva, I. M. (2017). Seismic crustal structure of the North China Craton and surrounding area: Synthesis and analysis. *Journal of Geophysical Research: Solid Earth*, *122*, 5181–5207. https://doi.org/10.1002/2016JB013848

Yang, Y., Ritzwoller, M. H., Levshin, A. L., & Shapiro, N. M. (2007). Ambient noise Rayleigh wave tomography across Europe. *Geophysical Journal International*, *168*(1), 259–274. https://doi.org/10.1111/j.1365-246X.2006.03203.x

Yegorova, T. P., & Starostenko, V. I. (2002). Lithosphere structure of Europe and Northern Atlantic from regional three-dimensional gravity modelling. *Geophysical Journal International*, *151*(1), 11–31. https://doi.org/10.1046/j.1365-246X.2002.01728.x

Zhu, H., Bozdag, E., Duffy, T., & Tromp, J. (2013). Seismic attenuation beneath Europe and the North Atlantic: Implications for water in the mantle. *Earth and Planetary Science Letters*, *381*, 1–11. https://doi.org/10.1016/j.epsl.2013.08.030

Zhu, H., Bozdag, E., Peter, D., & Tromp, J. (2012). Structure of the European upper mantle revealed by adjoint tomography. *Nature Geoscience*, *5*(7), 493–498. https://doi.org/10.1038/ngeo1501

Zhu, H., Bozdağ, E., & Tromp, J. (2015). Seismic structure of the European upper mantle based on adjoint tomography. *Geophysical Journal International*, *201*(1), 18–52. https://doi.org/10.1093/gji/ggu492

Zuilhuis, A., & Nolet, G. (1994). Deep seismic expression of an ancient plate boundary in Europe. *Science*, *265*(5168), 79–81. https://doi.org/10.1126/science.265.5168.79